Cement and Concrete Composites 171 (2026) 106641

Contents lists available at ScienceDirect

Cement and Concrete Composites

journal homepage: www.elsevier.com/locate/cemconcomp

Elucidating the role of enforced carbonation and clinker reduction in PET fiber-reinforced strain-hardening cementitious composites (SHCC)

Ameer Hamza Ahmed [a,b,*], Anna Jose [b], Cesare Signorini [a,b], Marco Liebscher [a,b], Marko Butler [b], Viktor Mechtcherine [a,b]

[a] Cluster of Excellence CARE, TU Dresden and RWTH Aachen, Germany
[b] Institute of Construction Materials, TUD Dresden University of Technology, 01069 Dresden, Germany

ARTICLE INFO

Keywords:
SHCC
PET fiber
Alkaline degradation
LC^3
Enforced carbonation
Sustainability

ABSTRACT

In cement-based matrices, polyethylene terephthalate (PET) fibers are prone to alkaline hydrolysis, limiting their structural applicability in strain-hardening cementitious composites (SHCC). This study evaluates two mitigation strategies: (i) reducing matrix alkalinity through clinker substitution and (ii) applying enforced carbonation curing. Three limestone calcined clay cement (LC^3) matrices containing 50%, 35%, and 25% clinker by weight were prepared to generate systems with decreasing alkalinity levels. PET-reinforced LC^3 composites were subjected to accelerated steam-curing aging (40 °C, 100% RH) for 14, 28, 60, and 90 days to assess fiber degradation, fiber-matrix bond performance via single-fiber pull-out tests, and strain-hardening behavior via uniaxial tension tests. A subset of specimens additionally underwent enforced carbonation curing (20% CO_2, 70% RH, 24 h) before steam curing to evaluate its effectiveness in preserving fiber integrity.

Results revealed a strong dependence of PET stability on matrix composition: severe degradation occurred in LC^3-50, moderate in LC^3-35, and minimal in LC^3-25. Enforced carbonation effectively mitigated degradation across all matrices, with particularly pronounced benefits in higher-alkalinity systems (LC^3-50 and LC^3-35). In LC^3-25 composites, enforced carbonation was unnecessary and even detrimental, impairing matrix integrity, fiber-matrix bond strength, and strain-hardening performance. These findings suggest that approaches to mitigate fiber degradation must be tailored to the matrix composition. While enforced carbonation is crucial for high-clinker SHCC, where fibers are most at risk, it can be counterproductive in low-clinker systems. Overall, this research offers valuable insights for designing durable, sustainable SHCC reinforced with PET fibers.

1. Introduction

The imperatives of performance, durability, and sustainability are increasingly interconnected, and addressing them collectively is now an essential aspect of modern materials design. Considering these aspects separately is inadequate: a material optimized for social, economic, and environmental sustainability is of little value if it cannot perform reliably over time, while even the most durable and high-performance material may face limited adoption if sustainability considerations are ignored. Ensuring the long-term acceptance and success of advanced construction materials, therefore, requires balancing these imperatives.

Among high-performance materials, strain-hardening cementitious composites (SHCC) exemplify the inherent tension among performance, durability, and sustainability at the material level. These fiber-reinforced composites exhibit exceptional tensile ductility and tight crack-width control, achieving mechanical performance that significantly surpasses that of conventional concrete [1–6]. These characteristics enable their use in applications including the repair, retrofitting, strengthening, and protection of existing structures [7–11]. At the structural scale, the relatively small volumes required for these applications make SHCC an environmentally and economically reasonable alternative to conventional concrete solutions, and superior performance remains the primary objective. However, at the material scale, SHCC still face notable sustainability and durability challenges related to its fundamental composition [1,12,13].

The fine-grained matrix typically requires elevated Portland cement (PC) content, resulting in a higher embodied CO_2 footprint. Furthermore, the high PC content promotes continued hydration and progressive matrix densification by raising the proportion of reactive phases. This aging process can reduce pseudo-ductility, i.e., tensile strain

* Corresponding author. Cluster of Excellence CARE, TU Dresden and RWTH Aachen, Germany.
E-mail address: ameer_hamza.ahmed@tu-dresden.de (A.H. Ahmed).

https://doi.org/10.1016/j.cemconcomp.2026.106641
Received 13 January 2026; Received in revised form 16 March 2026; Accepted 20 April 2026
Available online 21 April 2026

capacity that is critical for SHCC functionality [14,15]. In addition, SHCC often rely on high-performance fibers that impose significant economic constraints, while the long-term durability of the composite depends on the sustained performance of these fibers under various environmental exposures [16–19]. Addressing these limitations could improve the sustainability and durability of SHCC while maintaining their superior performance, enabling broader applications, including new constructions.

Nonetheless, employing a fine-grained matrix is essential for effectively embedding discrete polymer microfibers and ensuring proper crack bridging. Additionally, the absence of coarse aggregates in SHCC is necessary to reduce the matrix's fracture toughness, enabling easier crack propagation. These microfibers have diameters in the tens of micrometers, lengths of less than 20 mm, and are incorporated at dosages of 2-3 vol%. Under tensile loading, these fibers serve to bridge newly formed cracks, facilitating the transfer of stress from the crack flanks to adjacent intact matrix regions. Provided that the fiber crack-bridging capacity exceeds the matrix cracking strength, successive microcracks continue to develop, leading to multiple cracking phenomena and strain-hardening behavior. This mechanism enables significant inelastic deformations and confers exceptional pseudo-tensile ductility and energy-absorption capabilities under both quasi-static and dynamic loading conditions.

To achieve strain-hardening performance, high-performance polymeric fibers such as polyethylene (PE) and polyvinyl alcohol (PVA) are commonly employed owing to their superior tensile strength and Young's modulus [17–23]. While effective, these fibers entail high production costs, complex manufacturing processes, and substantial embodied energy and carbon emissions, further raising sustainability concerns for SHCC [24]. By contrast, polypropylene (PP) and polyethylene terephthalate (PET) fibers are more cost-effective due to simpler production pathways [25]. Despite their lower strength and Young's modulus – and their greater propensity for plastic deformation – our recent work demonstrates that PP fibers can still deliver robust strain-hardening when embedded in deliberately compliant, low-clinker matrices engineered to have reduced matrix strength [26].

The present study builds on these insights by evaluating PET fibers as a sustainable, cost-effective substitute for PE and PVA in SHCC. PET is the most widely produced and recycled synthetic fiber globally [27], and offers cost competitiveness comparable to PP, while offering improved wettability that can enhance fiber-matrix bonding and mechanical performance [24,28]. A critical limitation of PET, however, is its susceptibility to alkaline degradation in cementitious environments – manifested as progressive diameter reduction, molecular-weight decline, and surface pitting, collectively expediting tensile strength loss – which compromises long-term performance [29–34]. Our previous research demonstrated that PET fibers immersed in cement pore solutions at a pH of 12.5 undergo rapid degradation [35]. Specifically, tensile strength reductions of about 7.6%, 11.7%, 13.6%, and 24.7% were recorded after 7, 14, 28, and 60 days of exposure, respectively. The pronounced strength loss observed during the early stages of exposure underscores PET fibers' high susceptibility to alkaline environments and raises important concerns about the long-term durability of PET-reinforced cementitious materials. Comparable durability constraints also affect other appealing options, including natural and glass fibers, limiting their practical deployment in cementitious materials despite their favorable mechanical, economic, and environmental credentials [36–38].

To address these challenges and harness the substantial sustainability advantages of PET fibers, this study explores two strategies to reduce their degradation in SHCC:

(i) developing low-alkalinity (low-clinker) matrix formulations; and
(ii) applying enforced carbonation curing.

Besides mitigating alkali-induced degradation of PET fibers in SHCC, these methods also aim to stabilize matrix aging, helping to preserve the composite's strain-hardening properties.

1.1. Low-alkalinity matrix design

Partial replacement of PC with pozzolanic materials is an effective route to low-carbon, low-alkalinity binder systems [39–41]. Conventional PC matrices attain high alkalinity through portlandite ($Ca(OH)_2$) release during hydration, which elevates pH, and from alkali oxides (*e.g.*, Na_2O, K_2O) in the anhydrous cement. Lowering PC content proportionally lowers the concentration of these alkalis. In parallel, pozzolanic additions – typically amorphous siliceous or aluminous phases – further decrease alkalinity by consuming portlandite via pozzolanic reactions [42]. Accordingly, supplementary cementitious materials (SCMs) such as fly ash, silica fume, metakaolin, and natural pozzolans enable the development of low-alkalinity binders.

A particularly promising low-carbon cementitious binder is limestone calcined clay cement (LC^3), a ternary system capable of replacing $\geq$50 wt% of PC [43–45]. LC^3 leverages the combined benefits of calcined kaolinitic clay and natural limestone – both abundant and economical resources – to substantially reduce PC usage while maintaining favorable mechanical properties and durability. Importantly, LC^3 offers considerable environmental advantages, including improved embodied energy metrics and a reduced carbon footprint, thereby elevating the sustainability profile of cement-based construction materials [46–48].

Beyond sustainability advantages, substituting PC with limestone and calcined clays in LC^3, and, more broadly, incorporating fine mineral additives into blended cements confer anti-aging properties to the matrix, which are especially beneficial for SHCC. These effects mainly result from the “filler effect," which triggers two complementary mechanisms that stimulate hydration and ensure long-term stability [49–51]:

(a) *Nucleation enhancement*, where the fine particles in SCMs provide additional nucleation sites, accelerating early-stage clinker hydration; and
(b) *Dilution effect*, where at a fixed water-to-binder ratio, replacing cement with SCMs increases the effective water-to-cement ratio and available pore spaces, facilitating the precipitation of hydrates and pozzolanic phases and, in turn, raising the ultimate degree of hydration.

These effects intensify as PC substitution increases. In the authors' prior work, an LC^3-25 system consisting of 25 wt% PC and 75 wt% calcined clay and limestone, achieved complete clinker hydration and pozzolanic reaction within 28 days, owing to the pronounced “filler effect”. This was confirmed by the absence of unreacted clinker phases and portlandite in XRD-Rietveld analyses [52]; thereby conferring anti-aging characteristics from a hydration perspective and ensuring mechanical stability beyond 28 days [35].

1.2. Enforced carbonation

Although reducing PC content with SCMs effectively lowers matrix alkalinity, this alone is often not enough to prevent alkali-sensitive fiber degradation in SHCC. Even at lower PC levels, alkaline hydrolysis can occur if the matrix provides sufficient activation energy to initiate and progress fiber deterioration [42]. Moreover, extensive clinker substitution can compromise matrix strength and weaken the fiber-matrix interface, thereby diminishing the strain-hardening response of SHCC [26]. Balancing mechanical performance, durability, and sustainability, therefore, requires complementary strategies.

Carbonation of cementitious systems has been extensively studied, with early investigations primarily focusing on its detrimental effects on steel-reinforced concrete. By reducing pore solution pH – sometimes to values as low as 8.3 [53,54], below the depassivation threshold of

reinforcing steel – carbonation promotes the initiation and progression of steel corrosion, thereby compromising structural durability. More recently, however, its potential benefits have been recognized in cementitious systems without metallic reinforcement. In such matrices, dissolved CO_2 reacts with calcium-bearing phases to form $CaCO_3$, thereby enabling permanent mineral sequestration and positioning cement-based materials as viable carbon capture and storage (CCS) systems [54–57]. Enforced carbonation further strengthens this potential by facilitating the recycling of end-of-life concrete, reactivating cementitious fines for use as SCMs, and valorizing reclaimed aggregates as fillers [58–62], thereby directly supporting circular economy goals in the construction sector.

In SHCC, the role of enforced carbonation remains largely unexplored. Yet, it holds significant promise for enabling the use of economically and environmentally sustainable, but alkali-sensitive, fibers such as E-glass, natural fibers, and PET. Many fibers within these types create preferential pathways in the matrix, acting as conduits that facilitate deeper CO_2 diffusion. This enhances CO_2 sequestration by enabling more extensive and uniform CO_2 ingress while reducing the reliance on energy-intensive pressurization, hence improving the overall sustainability profile of SHCC [63]. A limited yet growing body of research [63–65] reports environmental, economic, and mechanical benefits of enforced carbonation in SHCC systems, along with mechanical improvements attributed to $CaCO_3$ deposition at the fiber-matrix interface, thereby strengthening bonding. While recognizing the documented benefits of carbonation curing of cementitious composites in terms of mechanics and the environment, this study delves deeper by assessing its effectiveness as a targeted mitigation strategy against the alkaline degradation of environmentally favorable fibers, such as PET, while maintaining the long-term mechanical integrity of SHCC. Demonstrating the viability of this approach could facilitate broader adoption of alkali-sensitive fibers in the construction sector.

2. Materials

2.1. Raw materials

Commercially produced, locally accessible raw materials were used in this study. Portland cement CEM I 52.5 R (Holcim Pur 5 R) with rapid strength development was sourced from Holcim GmbH, Lägerdorf, Germany. An industrially calcined clay with low kaolinite content (~25 wt% before calcination) was provided by Liapor GmbH & Co. KG, Hallerndorf, Germany. Limestone powder ("Saxodol 90 LE") was supplied by sh Minerals GmbH, Heidenheim/Brenz, and high-purity gypsum by Grüssing GmbH, Germany. Fine quartz sand (60-200 μm; Strobel Quarzsand, Germany) served as the aggregate.

To ensure uniform fiber dispersion and maintain fresh-mix workability, a viscosity-modifying agent (Unterwasser-Compound 100, Sika®, Germany) and a polycarboxylate ether (PCE)-based superplasticizer (MasterGlenium ACE 460, Master Builders Solutions, Germany) were incorporated. Appendix A provides the chemical composition (Table A1), mineralogical characteristics (Table A2), and physical properties (Fig. A1) of all mixture constituents.

ADVANSA GmbH (Germany) supplied PET fibers. For fiber-matrix bond evaluation via single-fiber pull-out tests, continuous PET filaments (ADVA®Tow) were manually cut to the required lengths, and for reinforcing SHCC, 18 mm chopped PET fibers (ADVA®Shortcut) were used. The fiber's physical and mechanical properties, obtained from the manufacturer [66] and supplemented with the experimental data from a prior study conducted on the same batch of PET fibers utilized herein [35], are summarized in Table 1.

2.2. Mixture design

Three SHCC matrices were formulated – LC^3-50, LC^3-35, and LC^3-25 – containing 50, 35, and 25 wt% Portland cement clinker, respectively.

Table 1
Physical and mechanical properties of PET fibers from the manufacturer's datasheet [66]; values in parentheses are the authors' measurements reported previously [35].

Fibers	PET
Manufacturer, country	ADVANSA, Germany
Brand name	ADVA® Shortcut, ADVA®Tow
Length (mm)	18 (*shortcut*), long (*tow*)
Diameter (μm)	18, (17 ± 0.69)
Tensile strength (MPa)	N.A, (584.8 ± 34.8)
Young's modulus (GPa)	N.A, (12.3 ± 6.9)
Fiber elongation (%)	34, (31.8 ± 3.3)
Density (g/cm^3)	1.37
Color	Semi-dull white
Melting point (°C)	~250

The remaining binder fraction comprised calcined clay and limestone at a fixed 2:1 mass ratio. To ensure adequate sulfation, 3 wt% gypsum (relative to the PC content) was added to each mix; this dosage has been previously validated for all three compositions [52].

A constant water-to-binder ratio (w/b) of 0.40 – intentionally higher than typical for SHCC – was adopted for two reasons: (i) the resulting higher porosity facilitates crack initiation, which is beneficial when employing low-strength and compliant fibers such as PET; and (ii) increased pore volume provides ample space for hydrate and pozzolanic product precipitation, promoting a higher overall degree of hydration, thereby supporting long-term matrix stability and mitigating aging effects.

The sand-to-binder ratio (s/b) was limited to 0.23 to reduce matrix fracture toughness and facilitate the propagation of multiple cracks [67]. PET fibers were incorporated at a fixed dosage of 2.5 vol% in all mixtures. The detailed mixture compositions (in kg/m^3) are provided in Table 2.

The mixing procedure for SHCC specimens used in compression and uniaxial tension, and for fiber-free mortars prepared for single-fiber pull-out tests, followed the standardized protocol established in a prior study [68].

3. Experimental methods

3.1. Compression test

Compressive strength development of carbonated (*C*) and non-carbonated (*NC*) LC^3-based PET-reinforced SHCC was evaluated in accordance with EN 196-1 [69]. Compression tests were conducted using a load-controlled EU 20 hydraulic testing machine (Germany) at a constant loading rate of 2.4 kN/s on cubic specimens measuring 40 × 40 × 40 mm. To ensure statistical robustness, at least six specimens were tested for each curing condition and age (as detailed in Section 3.4).

3.2. Single fiber pull-out test

Single-fiber pull-out (SFPO) specimens were produced using a custom mold adapted from prior studies, with minor modifications [70,

Table 2
Various LC^3-PET SHCC mixture compositions, in kg/m^3.

Raw ingredients	LC^3-50-PET	LC^3-35-PET	LC^3-25-PET
Cement	584	404	286
Limestone	187	245	282
Calcined clay	375	490	564
Gypsum	18	12	9
Quartz sand	262	259	257
Fibers	34	34	34
Water	467	462	458
Superplasticizer	4	5	6
VMA	4	4	4

71]. The mold comprised two horizontal support plates with a 4 mm-thick spacer inserted between them to define the fiber embedding length. The assembly was secured with lateral screws. PET fibers were aligned equidistantly across the support plates and fixed at both ends using adhesive tape. Two mm-thick top plates were then mounted above the support plates. As the spacer was two mm shorter than the support plates, a four mm-deep cavity was formed for matrix pouring. All mold surfaces in contact with the matrix were wax-coated to ease demolding, and the cavity ends were sealed with tape to prevent matrix leakage. The matrix was then cast into the cavity, and the molds were sealed in plastic bags for 24 h to allow the matrix to harden. The following day, before demolding, one side of the protruding fibers was cut using a sharp blade, while the other protruding side defined the free fiber length. The hardened matrix beam, containing fibers protruding from one side only, was then demolded and cut into $4 \times 4 \times 4$ mm^3 cubic specimens using a precision thin saw. Each specimen contained a single, centrally embedded fiber, prepared for individual pull-out testing. The complete preparation process and mold configuration are illustrated in Fig. 1.

The SFPO tests were conducted using a 10 N load cell mounted on a Zwick/Roell Z1445 testing machine, operated under displacement control at a constant rate of 0.05 mm/s. To anchor the fiber during testing, a small paper frame was used to clamp the free fiber end, effectively reducing the free length from 4 mm to 2 mm. The matrix block was affixed to a plastic mounting block and attached to the upper grip of the testing machine using a high-speed UV adhesive, which cured within 10-15 s under UV light. Meanwhile, the paper frame holding the fiber was mechanically fastened to a clamp on the lower side. The whole experimental setup is illustrated in Fig. 2.

Twenty specimens were prepared per fiber-matrix combination and curing condition. Owing to occasional handling losses or testing inconsistencies, 16-18 valid tests were typically obtained; in the least favorable cases, at least eight valid results were analyzed.

3.3. Uniaxial tension test

Uniaxial tensile tests on LC^3-based, PET-reinforced SHCC were performed on dumbbell-shaped specimens (total length 250 mm; gauge length 100 mm). The cross-section tapered smoothly from 24 × 40 mm in the gauge to 40 × 40 mm in the clamping regions. Detailed geometry and setup are provided elsewhere [72,73]. Tests were carried out under displacement control at a rate of 0.05 mm/s using an Instron 8802 universal testing machine equipped with custom-built mechanical grips to ensure rigid boundary conditions.

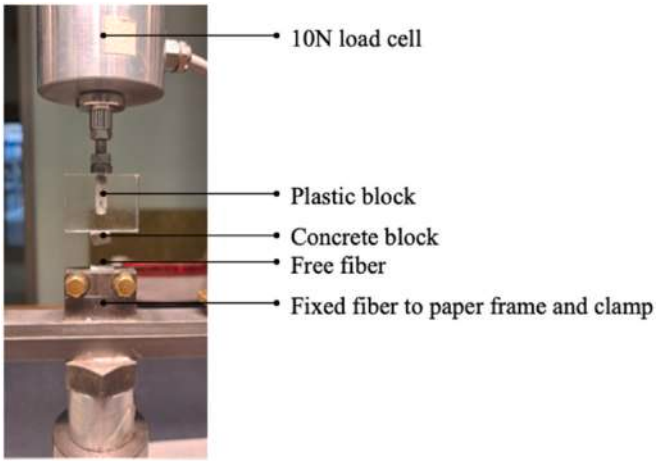

Fig. 2. Testing configuration in Zwick/Roell 1445 for SFPO test.

For in-situ crack monitoring, specimens were coated with a white base and fine black speckle pattern, and imaged using a stereo DIC system (Carl Zeiss GOM Metrology GmbH) with synchronized illumination. Acquisition was triggered at an applied load of 500 N; images and load-displacement data were recorded at 2 Hz using Aramis Professional software. Axial strain was computed from two virtual extensometers spanning the gauge section by tracking speckle displacements across successive frames. Crack widths were evaluated with virtual calipers at each visible crack within the gauge length, whereas the number of cracks was manually counted at the point of ultimate tensile strain.

A minimum of three to four replicates were tested for each matrix/

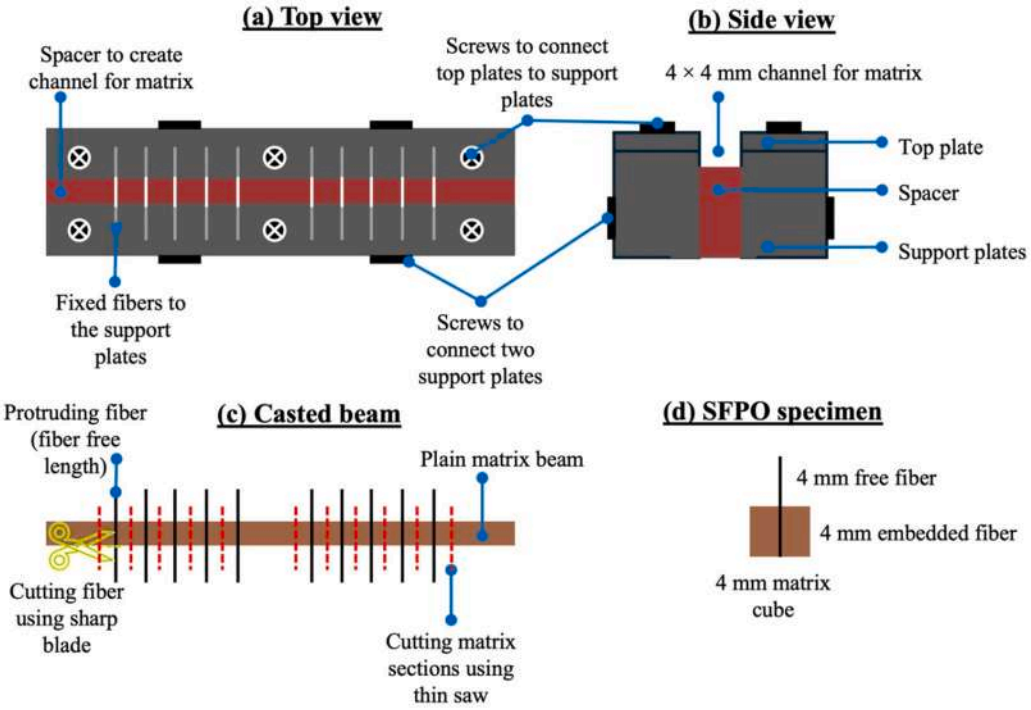

Fig. 1. Schematic diagram showing the mold used and the fabrication process of single fiber-pullout specimens.

fiber combination and curing condition to ensure statistically reliable mechanical performance data.

3.4. Curing methods and duration of test samples

Fig. 3 summarizes the curing regimes used to simulate accelerated aging of LC^3-PET SHCC. For the non-carbonated (*NC*) series, specimens were kept in molds for 1 day, then demolded and seal-cured at 22 °C for 5 additional days (total age 6 days). Thereafter, they were placed in a fog chamber at 40 °C and 100% RH for 14, 28, 60, or 90 days, yielding test ages of 20, 34, 66, and 96 days, respectively.

For the carbonated (*C*) series, two additional steps preceded fog curing. After 1 day in molds and 3 days of sealed curing at 22 °C, specimens were unsealed and preconditioned in a ventilated oven at 40 °C for 1 day to partially remove free water and open the pore structure for deeper CO_2 ingress. They were then carbonated for 1 day in a chamber at 20 °C, 70% RH, and 20% CO_2, followed by fog-chamber curing under the same conditions and for the exact durations as the *NC* series.

The chosen preconditioning and carbonation parameters (temperature, duration, humidity, and CO_2 concentration) were selected in the absence of standardized guidelines in the literature. While it is well established that these parameters markedly influence carbonation rate, no universally standardized protocol exists. The determination of optimal conditions is highly contingent on various complex variables, including specimen geometry (*e.g.*, volume and surface-area-to-volume ratio), mixture composition, and the degree of hydration at the time of treatment [74,75]. Nonetheless, identical drying and carbonation-curing conditions were applied to all composite variants, namely LC^3-50-PET, LC^3-35-PET, and LC^3-25-PET, to ensure methodological consistency and comparability, despite the variations in binder composition and resultant hydrated microstructures. Consequently, carbonation was only partial in the denser, higher-clinker systems (LC^3-50 and LC^3-35), as elaborated in Section 4.1. Achieving complete carbonation in such systems would likely require more aggressive conditions, such as extended exposure times, higher CO_2 concentrations, or elevated pressure. However, due to the lack of protocols linking binder composition to optimal carbonation parameters, the present study did not pursue parameter optimization. Instead, the focus was placed on evaluating the effectiveness of carbonation curing in mitigating PET fiber degradation in LC3-based composites, a phenomenon reflected in the mechanical performance even under partial carbonation conditions, as discussed in Section 4.

One informed decision in this context was the implementation of early-age carbonation (*i.e.*, on day 5), motivated by previous findings indicating that PET fibers can lose nearly 8% of their tensile strength within the first seven days of exposure to an alkaline environment [35]. Accordingly, carbonation curing was applied before 7 days of hydration to protect the PET fibers.

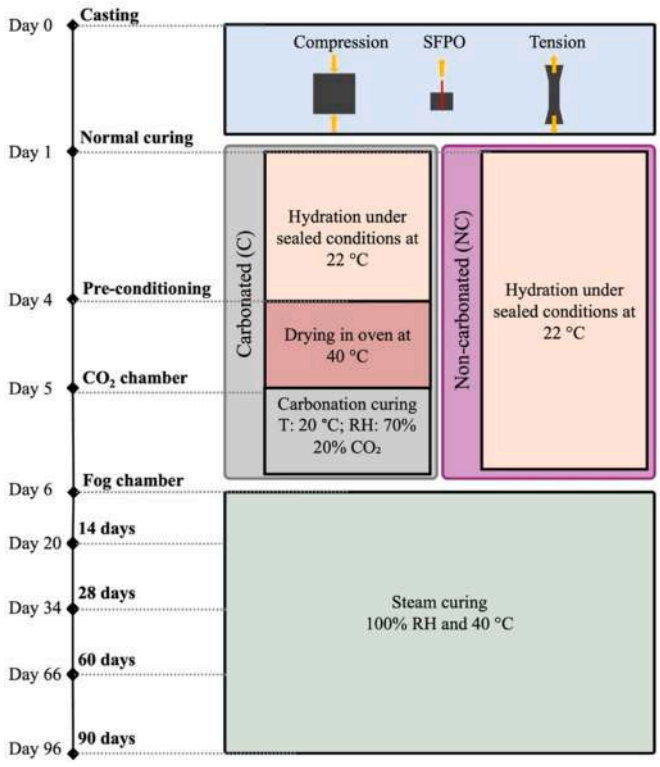

Fig. 3. Curing conditions and durations of specimens for accelerated aging.

3.5. Carbonation depth quantification

Following uniaxial tension testing, dumbbell-shaped specimens were dry-cut within the undamaged gauge region using a precision diamond saw, and cutting debris was removed with compressed air. The freshly exposed cross-sections were sprayed with phenolphthalein and thymolphthalein indicators to distinguish *C* from *NC* zones by color change. The carbonation depth was measured manually using edge distances A1, A2, B1, and B2 (Fig. 4), which were used to quantify the proportions of non-carbonated (X_{NC}) and carbonated (X_C) cross-sectional area.

4. Results and discussion

4.1. Carbonation depth and qualitative pH mapping

Fig. 5 shows the proportions of X_{NC} and X_C for *NC*- and *C*-series composites post-uniaxial tension tests on dumbbell-shaped samples. Ideally, X_{NC} and X_C fractions within the same matrix type should not vary with curing age, since all samples were carbonated simultaneously before steaming. However, some scatter appears, evident in Fig. 5(a–c, d), reflecting the natural heterogeneity of cementitious matrices and inevitable fabrication tolerances. It's important to note that the method used to estimate these quantities assumes a rectangular *NC* core, which slightly overestimates X_{NC} and underestimates X_C. This deviation from a perfect rectangle is evident in the specimens' actual cross-sections (Fig. 6).

While *NC* LC^3-50-PET and *NC* LC^3-35-PET remained completely non-carbonated, *NC* LC^3-25-PET exhibited moderate carbonation despite not being subjected to carbonation curing. This likely resulted from natural carbonation that occurred after removal from steam curing and before testing. The relatively open microstructure of the LC^3-25 matrix facilitated natural carbonation by allowing easier ingress of atmospheric CO_2. In contrast, for the *C* samples, a clear composition-dependent trend emerged: LC^3-50-PET exhibited the lowest X_C; LC^3-35-PET exhibited somewhat deeper CO_2 ingress; and LC^3-25-PET was carbonated entirely. This pattern corresponds to the degree of microstructural densification across various matrices, which shows a positive correlation with clinker content. Microstructural analysis using mercury intrusion porosimetry

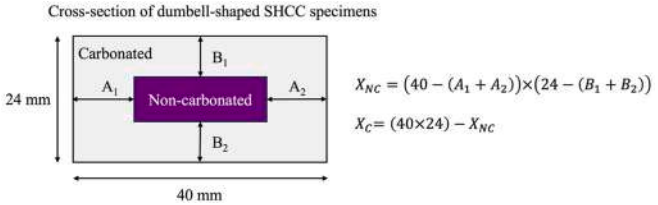

Fig. 4. A schematic diagram illustrating the method for measuring the carbonated cross-section (X_C) and non-carbonated cross-section (*XNC*) in dumbbell-shaped SHCC specimens.

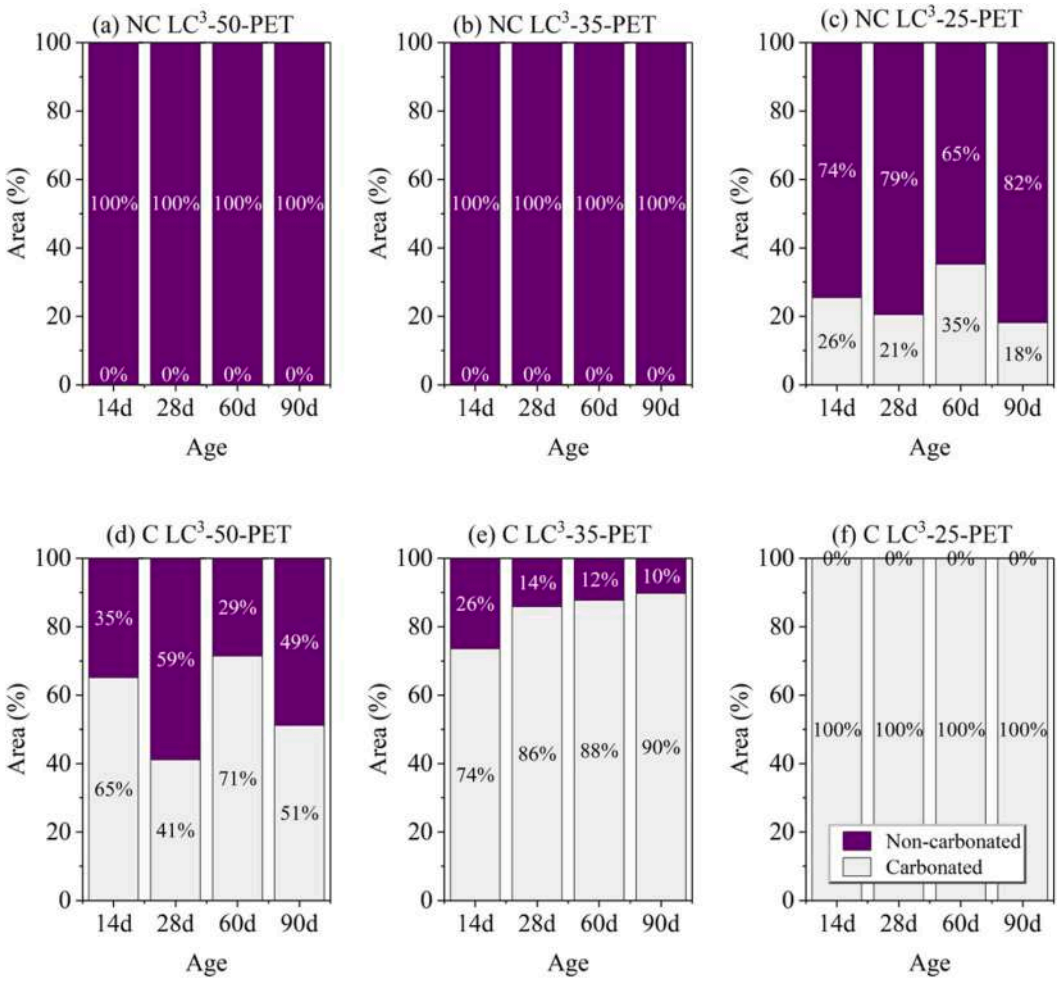

Fig. 5. Quantification of carbonated (X_C) and non-carbonated areas (X_{NC}) over time for various LC^3-PET composites: **(a–c)** non-carbonated (*NC*) samples; **(d–f)** carbonated (*C*) samples.

(MIP) reported in a previous study (see Figs.15 and 16 in Ahmed et al. [52]) indicates that the LC^3-50 matrix is denser due to its higher clinker content, which limits CO_2 diffusivity. This emphasizes that achieving complete carbonation in denser matrices like LC^3-50 requires more thorough pre-conditioning, such as longer drying times or higher temperatures, as well as more intense carbonation efforts, including extended exposure or increased pressure.

The rationale for employing both indicators stems from the distinct yet overlapping pH-sensitivity ranges of the two substances (*cf.* Fig. 6). Although this approach does not allow for precise pH quantification, the dual-indicator method proved effective for rapid qualitative assessment of internal alkalinity in these matrices after accelerated aging. For instance, in the *NC* LC^3-25-PET, faint blue coloration indicated a pH range of approximately 9.3-10.5, consistent with lower alkalinity resulting from elevated PC replacement and consumption of portlandite via pozzolanic reaction. Conversely, *C* LC^3-25-PET exhibited no color change with either indicator, indicating complete carbonation and a pH below 8.2. Meanwhile, the pH levels of *C* and *NC* LC^3-35-PET and LC^3-50-PET specimens consistently exceeded 10.5, as evidenced by more intense color shifts.

Furthermore, a comparison of Fig. 6 with Fig. B1 in Appendix B, which shows prismatic cross-sections of various LC^3 mortars without fibers, suggests that the incorporation of PET fibers promotes deeper CO_2 penetration. Visual inspection indicates that the fibers may serve as pathways facilitating CO_2 ingress into the matrix, consistent with mechanisms reported in previous studies [63]. This phenomenon becomes particularly pronounced when contrasting LC^3-25-PET with the corresponding fiber-free LC^3-25 mortar. Under identical carbonation conditions and matrix composition, LC^3-25-PET exhibits complete carbonation, whereas the LC^3-25 specimen retains an *NC* core.

This comparison remains qualitative due to differences in specimen geometry: the fiber-reinforced samples in Fig. 6 have a dumbbell shape with a smaller cross-section (40 × 24 mm^2), whereas the mortars in Fig. B1 are prismatic (40 × 40 mm^2). Nevertheless, the differences in carbonation depth appear more strongly associated with fiber presence than with specimen geometry. This is further supported by the carbonation front morphology: fiber-free mortars show a relatively uniform front consistent with the specimen shape, while fiber-reinforced samples display a more irregular front, likely reflecting localized CO_2 ingress along randomly distributed fibers.

Although qualitative, these observations suggest that PET fibers may facilitate CO_2 transport and promote deeper carbonation in cementitious composites, without needing energy-intensive preconditioning and carbonation processes to achieve similar carbonation depths in fiber-free mortars.

4.2. Compression test

Fig. 7 shows the development of compressive strength in the investigated LC^3-based composites across various curing durations. Additionally, Table C1 in Appendix C presents tabular data indicating the percentage decrease relative to *NC* LC^3-50-PET, thereby highlighting differences in mixture composition and curing regimes (*NC vs. C*).

Among various matrix compositions, compressive strength increases

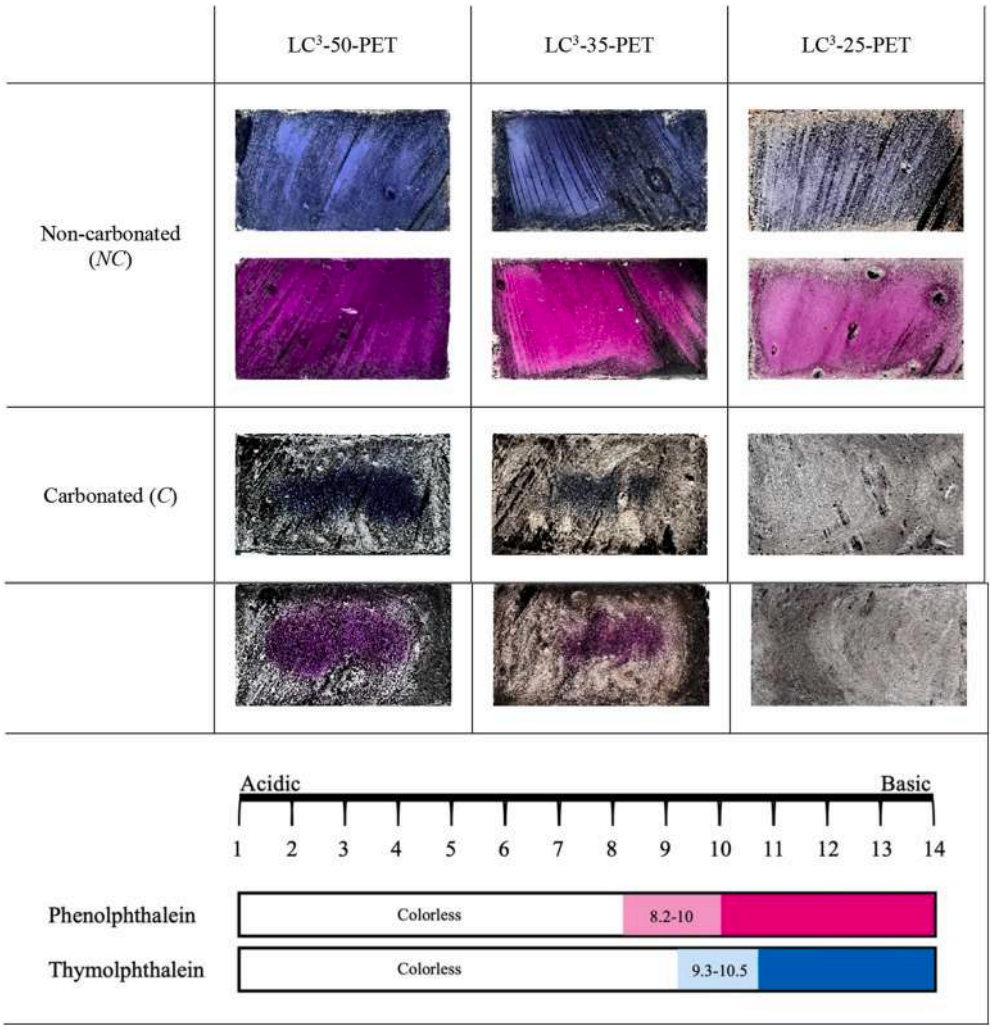

Fig. 6. Phenolphthalein and thymolphthalein applied to cut surfaces of *C* and *NC* LC^3-based PET-reinforced SHCC samples (gauge region) for qualitative pH evaluation and carbonation depth measurement.

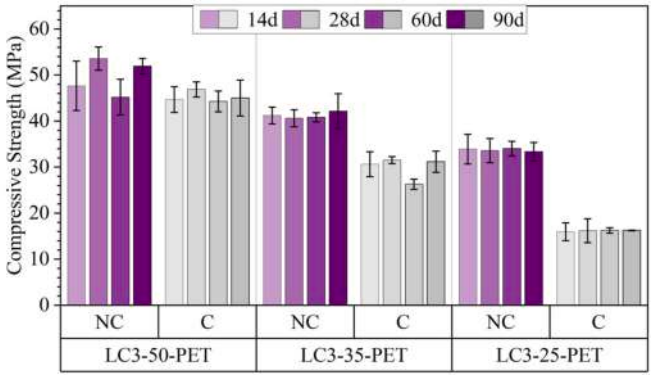

Fig. 7. Compressive strength of LC^3-50-PET, LC^3-35-PET, and LC^3-25-PET composites after 14, 28, 60, and 90 days of steam curing (*NC*, purple shade) and with prior carbonation curing (*C*, gray shade). (For interpretation of the references to color in this figure legend, the reader is referred to the Web version of this article.)

with higher clinker content: LC^3-50-PET surpasses LC^3-35-PET, which in turn surpasses LC^3-25-PET. In other words, greater PC replacement decreases matrix strength. These findings are consistent with our prior research, which emphasized that the advantages of incorporating calcined clay and limestone – specifically, the increase in strength attributed to the "filler effect" – diminish beyond approximately 30 wt% replacement of PC [52].

Furthermore, across all compositions, the only-hydrated specimens (*NC* series) exhibited higher compressive strengths than their carbonated counterparts (*C* series). Moreover, the *NC-C* strength gap widened as clinker content decreased during the transition from LC^3-50-PET to LC^3-35-PET and further to LC^3-25-PET. This is attributed to the extent of carbonation in the composites. In the LC^3-50-PET and LC^3-35-PET samples, the carbonation process was incomplete, resulting in a purely hydrated core that is stronger than the surrounding carbonated shell. Consequently, the sample retains most of its strength. If complete carbonation had been achieved, lower compressive strength values would likely have been recorded.

Interestingly, carbonation-induced strength loss was more pronounced in diluted blends than the reduction attributable solely to clinker replacement, as indicated by the percentage decrease relative to *NC* LC^3-50-PET (Table C1). Reducing the clinker content from LC^3-50 to LC^3-35 (a 30% decrease) resulted in a 9.7-24.2% reduction in compressive strength across the examined curing ages. In contrast, the carbonated counterpart, *C* LC^3-35-PET, exhibited substantially greater reductions of 35.6-41.8%. This decline exceeds that observed for *NC* LC^3-25-PET, which contains 50% less clinker than LC^3-50-PET but shows a strength reduction of only 24.8-37.3%. The effect is further amplified by additional dilution of the cementitious system with calcined clay and

limestone, as *C* LC^3-25-PET exhibits a 64.0-69.8% reduction in compressive strength relative to *NC* LC^3-50-PET across the examined curing periods.

The observed reduction in compressive strength due to carbonation is mainly attributed to changes in the hydrate phase assemblage and the intrinsic pore-solution chemistry characteristic of LC^3 binders. Interactions with CO_2 notably impact both [57,75]. In cement-based systems, carbonation triggers a sequence of decalcification reactions that modify key hydration products, leading to the precipitation of calcium carbonate as the dominant carbonation byproduct. These chemical transformations are accompanied by microstructural densification, driven by the differing molar volumes of hydrated *vs.* carbonated phases [75–77]. Specifically, carbonation of residual anhydrous clinker phases – such as alite (C_3S) and belite (C_2S) – increases solid volume and microstructural densification [78]. Similarly, carbonation of portlandite (CH) causes densification due to calcite's (36.9 cm^3/mol) larger molar volume compared to portlandite (33.0 cm^3/mol) [75]. Conversely, the decalcification of C-(A)-S-H and ettringite (AFt) during carbonation leads to microstructural shrinkage, known as decalcification shrinkage [77,79,80]. The three LC^3-based matrices investigated in this study contain limited residual anhydrous clinker phases and portlandite, due to the "filler effect" and pozzolanic reactivity of the SCMs, respectively, but are rich in C-(A)-S-H and ettringite phases [52]. Consequently, net decalcification shrinkage predominates, diminishing microstructural densification and compressive strength in the carbonated regions. Furthermore, as the PC content decreases from LC^3-50 to LC^3-35 and LC^3-25 matrices, these adverse effects become more pronounced, resulting in greater strength loss upon carbonation.

A closer examination of the effect of curing age on compressive strength development reveals that, across all matrix variants, both the *NC* and *C* series attained near-final strength values by 14 days, with minimal changes observed thereafter. This behavior is indicative of the composites' anti-aging characteristics. Minor deviations, such as the slightly lower 60-day strength observed in *NC* LC^3-50-PET, are more plausibly attributable to experimental uncertainties than to intrinsic material behavior. The anti-aging response is primarily attributed to the accelerated curing conditions employed, wherein steam exposure enhanced both clinker hydration and pozzolanic activity. These effects are particularly prominent in SCMs-rich blends, which inherently promote rapid hydration kinetics due to their pronounced "filler effect". Importantly, this strength-stabilization trend appears unaffected by prior carbonation curing, indicating that accelerated steam curing drives near-complete consumption of reactive phases in both *C* and *NC* specimens.

Although these results indicate a strong anti-aging response, further investigation, such as Quantitative X-ray Diffraction (QXRD) and Thermogravimetric Analysis (TGA) under the same curing conditions, is needed for definitive proof. However, these analyses are beyond the scope of the current study.

Regarding PET fiber degradation in different LC^3-based matrices and the possible mitigating effect of carbonation curing, compressive strength results do not reliably reflect these influences. Therefore, the following sections analyze these aspects in more detail using single-fiber pull-out and uniaxial tensile tests, which directly measure how PET degradation or preservation affects the fiber-matrix bond and crack-bridging ability.

4.3. Single fiber pull-out test (SFPO)

Although SFPO experiments are conceptually straightforward, the resulting force-displacement responses are challenging to interpret – particularly when the intrinsic properties of the embedded fiber evolve over time. Alkaline attack on PET within the matrix induced progressive physico-mechanical changes, notably reductions in fiber diameter and tensile strength [35], whose severity increased with exposure duration. Since the fiber is embedded, its diameter cannot be accurately measured before testing, and any post-test thinning may be influenced by chemical degradation, plastic deformation, and Poisson's effect during pull-out. As a result, absolute pull-out force values (P) were used to assess fiber-matrix interaction, rather than relying on derived parameters such as in-situ tensile stress (σ) or interfacial bond strength (τ).

Four distinct failure mechanisms were identified during the SFPO experiments. The combination of variable matrix strength arising from different compositions and variations in the degree of PET degradation in the embedded zone strongly influenced their occurrence. A schematic representation of these four failure cases is shown in Fig. 8, based on trends observed in all corresponding force-displacement curves, which are compiled in Appendix D: Fig. D1 (PET fiber pull-out from LC^3-50, *NC* and *C* series); Fig. D2 (LC^3-35, *NC* and *C* series); and Fig. D3 (LC^3-25, *NC* and *C* series).

Case 1 represents the pure fiber pull-out mode. The initial segment of the *P-δ* curve reflects the compliance of both the fiber and the testing setup [81]. This phase concludes at the point where debonding and interfacial cracking begin, marked by a slope change. The maximum load corresponds to complete debonding between the fiber and the matrix, known as the peak debonding load (P_d), marking the formation of a fully developed interfacial crack [82]. Thereafter, the force decreases to the load corresponding to initiation of fiber pull-out (P_p), representing friction-based sliding resistance along the debonded interface, which diminishes progressively as the embedded fiber length decreases, eventually reaching zero upon complete fiber pull-out [83].

Case 2 represents the pure fiber rupture mode. The fiber-matrix interfacial zone plays a critical role in governing the fiber failure mechanism during SFPO tests. Specifically, the interplay between chemical adhesion and frictional bonding at the interface, relative to the fiber's intrinsic tensile strength, determines whether failure occurs by fiber pull-out or fiber rupture. When the embedment length is sufficiently large, or the matrix strength exceeds that of the fiber, the interfacial resistance may surpass the fiber's tensile capacity, increasing the likelihood of rupture before complete interfacial debonding occurs. In this case, the peak load corresponds to the in-situ load-bearing capacity of the fiber (P_f). This value is typically lower than the fiber's direct (ex-situ) tensile strength because matrix hardening can induce damage to the relatively soft fibers. Furthermore, even slight fiber inclination can introduce stress concentration or notching at the junction between the embedded and free fiber segments during pull-out, further weakening the fiber and promoting premature rupture [70].

Case 3 describes a mixed failure mode involving partial debonding at the fiber-matrix interface, followed by sudden fiber rupture before complete debonding/pull-out. This behavior was frequently observed in specimens with moderate PET degradation, which facilitated debonding initiation due to a slight reduction in diameter and triggered rupture due to loss of fiber load-bearing capacity. Consequently, the peak load in this case, corresponding to the fiber's in-situ load-bearing capacity (P_f), was lower than that in the pure fiber rupture mode as in *Case 2*, reflecting degradation-induced fiber weakening.

Severely degraded fibers also exhibited mixed failure modes, categorized as *Case 4*. In *Case 4(a)*, a portion of the embedded fiber ruptured within the matrix block, after which the residual fiber segment was pulled out. In this case, the pull-out resistance was minimal compared to the fully intact 4 mm embedded fiber, and both the fiber failure load (P_f) and pull-out load (P_p) were significantly lower than in earlier cases. A rarer sequence, *Case 4(b)*, involved interfacial debonding followed by partial pull-out and subsequent rupture. Finally, *Case 4(c)*, more frequently observed, involved degradation-induced diameter reduction that promoted partial debonding, followed by rupture within the embedded matrix region due to diminished load-bearing capacity, and eventually a residual pull-out phase. Variations in the occurrence of these failure modes likely reflect spatial differences in degradation severity, matrix heterogeneity, and normal experimental scatter (*e.g.*, slight fiber misalignment).

Fig. 9 presents representative *P-δ* curves from the pull-out

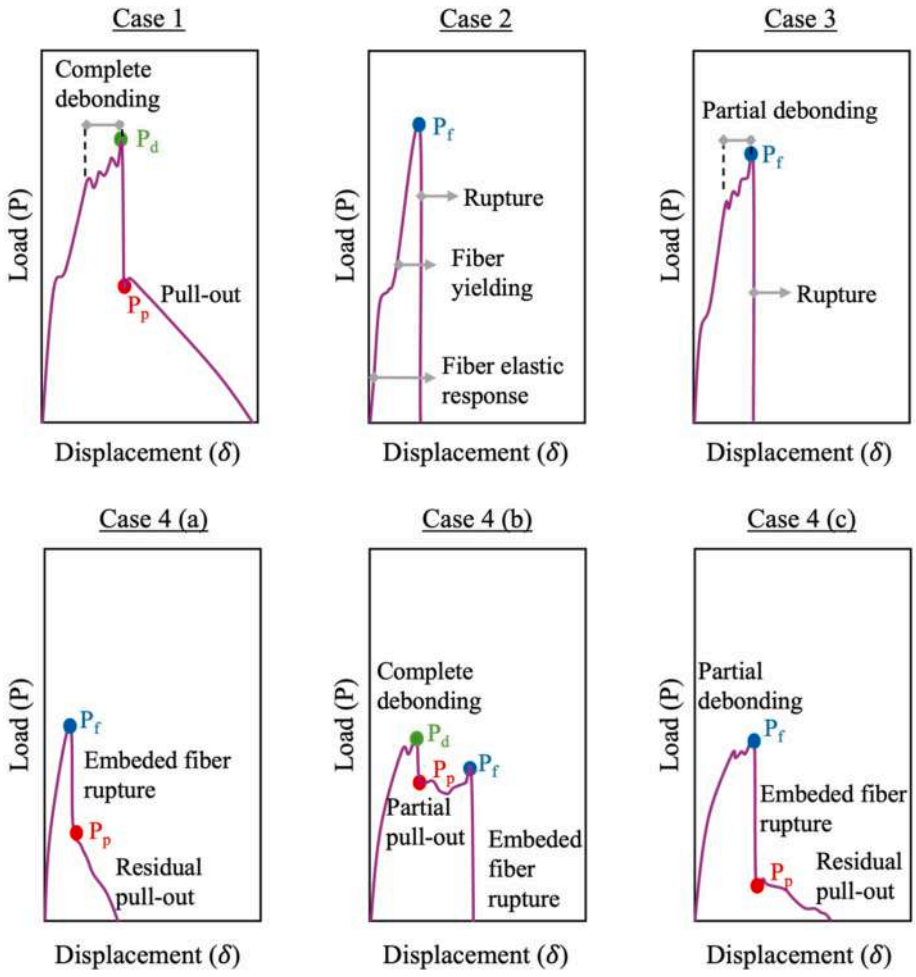

Fig. 8. Schematic illustration of various pull-out responses and PET fiber failure modes observed in the experimental data.

experiments. The load is expressed in Millinewtons (mN) due to the small magnitude of the recorded values. Additionally, the graphs include ex-situ PET tensile load-bearing capacity from single fiber tensile tests reported in our previous study [35]. The representative curves were selected based on two criteria: (i) the dominant failure mode in each tested series (*Cases 1-4*), as indicated in the legend of each graph; in cases where two modes occurred with equal frequency, the representative curve for pure fiber pull-out or rupture was selected, and (ii) within the dominant mode, the curve that most closely matched the mean values summarized in Table 3.

NC LC^3-50-PET specimens showed a continuous decline in fiber-matrix interfacial performance with age, mainly due to ongoing alkaline degradation of the embedded PET. The in-situ fiber capacity (P_f) decreased by 11.8%, 58.6%, and 63.6% after 28, 60, and 90 days of steam curing, respectively, compared with the values at 14 days. Interestingly, this degradation progressed more slowly in *NC* LC^3-35-PET specimens, consistent with the system's lower alkalinity. In fact, P_f remained nearly unchanged for the first 14 and 28 days; only then did it decrease by 7.2% and 30% at 60 and 90 days. A similar trend was observed for the pull-out load (P_p) in these specimens.

Remarkably, no observable degradation was detected in any metrics (P_f, P_d, or P_p) across all ages in their carbonated counterparts, *i.e.*, *C* LC^3-50-PET and *C* LC^3-35-PET. In addition, these specimens predominantly transitioned from the fiber-rupture mode observed in their *NC* counterparts to a pure fiber-pull-out failure mode. This shift is attributed to a loss of matrix strength due to carbonation (as discussed in compression test results), which manifested locally as reduced confinement/density in the fiber-matrix channel, thereby lowering interfacial bond strength and favoring debonding/pull-out.

It is important to note that the pull-out specimens were likely fully carbonated due to their small dimensions [84], or, at the very least, the fiber-matrix channel spanning the full specimen thickness – which provides CO_2 ingress/egress – was thoroughly carbonated in all LC^3 blends regardless of matrix composition.

In general, many studies report densification of the fiber-matrix interface upon carbonation [84–89]. However, the findings of the present study demonstrate that this is not always true; rather, the effect is composition-dependent. As discussed earlier, in matrices rich in C-(A)-S-H and AFt but deficient in portlandite and residual unhydrated clinker, carbonation does not produce net densification. This is reflected in the bond responses across all mixtures and is most clearly demonstrated by LC^3-25, where PET does not degrade due to the matrix's low alkalinity, enabling a direct comparison of *C* and *NC* states. In *NC* LC^3-25, failure is typically governed by pull-out, consistent with the matrix's intrinsically low strength. After carbonation, both P_d and P_p decrease substantially relative to *NC*, indicating carbonation-induced microstructural rarefaction rather than fiber degradation.

Fig. 10 (b-g) shows scanning electron microscopy (SEM) micrographs of fiber ends extracted after SFPO tests from the matrix-embedded portions of the fibers, compared with the as-received PET fiber in Fig. 10 (a), illustrating the extent of PET degradation. The degradation is categorized into three levels: (i) limited degradation – characterized by localized surface pits (micro-spalling); (ii) significant degradation – where pitting covers the entire fiber surface; and (iii) severe degradation – featuring extensive pitting along with a noticeable reduction in fiber diameter. If none of these signs are present, it suggests

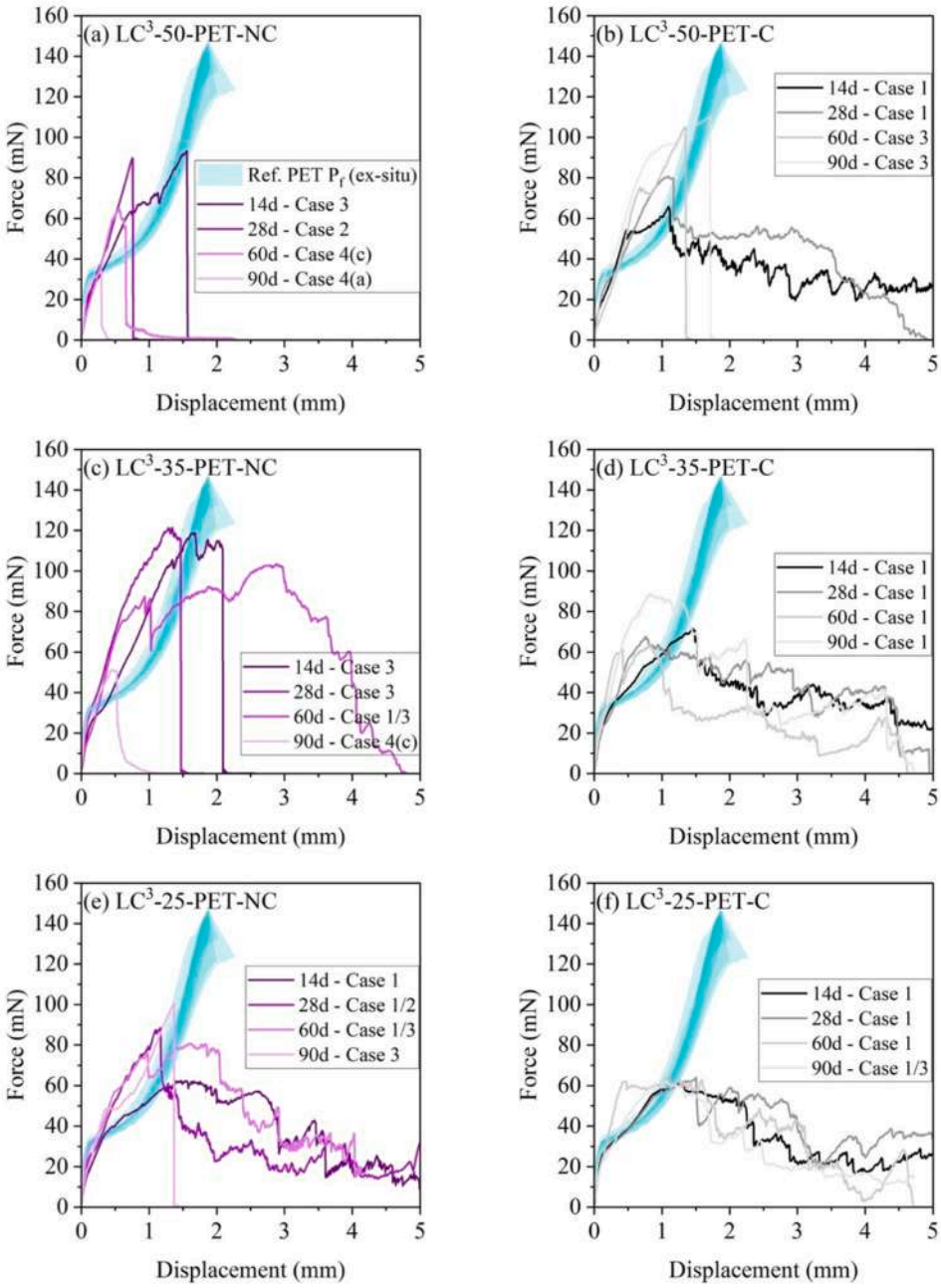

Fig. 9. Representative pull-out response curves, with the dominant cases highlighted in legends for each fiber-matrix pairing from the *C* and *NC* series cured for different durations.

that PET did not degrade.

The SEM micrographs reveal that degradation occurs only in the PET fibers within the *NC* series of the LC^3-50 and LC^3-35 matrices. The observed surface pitting results from the attack of strong alkali hydroxides, present in the pore solution, on the PET polymer chains. This chemical attack breaks down PET into terephthalic acid salts (precipitates/film forming) and ethylene glycol (soluble) [90,91]. This degradation is progressive: the longer PET fibers are exposed to the alkaline environment, the more pronounced the surface pitting becomes. This continuous breakdown of polymer chains proceeds from the surface inward, resembling a peeling effect, which explains the observed reduction in fiber diameter after severe pitting.

In contrast, the LC^3-50 and LC^3-35 matrices from the *C* series showed no apparent signs of alkaline degradation, indicating that carbonation effectively reduced the pH of the pore solution in these systems. However, traces of scratching damage and localized fibril peeling were visible on the surfaces, suggesting a friction-dominated failure mode, *i.e.*, pure pull-out. Similar scratch marks were also observed, to a lesser extent, on PET fibers pulled out from the *NC* LC^3-25 matrix, where no pitting or diameter reduction was evident. Yet confirming again the notion that a low-clinker matrix can protect alkali-sensitive fibers from degradation due to its inherently low alkalinity, even without carbonation.

Notably, *C* LC^3-25 exhibited a mineral coating on the fiber surface, particularly at longer curing ages, which is presumed to be calcium carbonate. This suggests that PET may act as a nucleation template for carbonate precipitation, with interfacial sliding occurring at the coating-matrix interface rather than directly at the fiber-matrix interface.

Table 3
Summary of key parameters derived from single fiber pull-out tests of PET fibers within different LC^3 matrices after various steam curing durations, with and without prior carbonation curing (*C* and *NC*, respectively). Standard deviations are reported in parentheses.

Matrix	Age	In-situ load bearing capacity - P_f [mN]		Max. debonding force - P_d [mN]		Force at initition of pull-out - P_p [mN]	
		C	NC	C	NC	C	NC
LC^3-50	14d	94.3[a] (–)	93.3 (9.3)	68.8 (16.1)	80.6[a] (–)	45.8 (15.6)	56.7[a] (–)
	28d	92.8 (20.3)	82.3 (12.2)	75.0 (17.6)	Undefined	56.6 (24.8)	Undefined
	60d	101.0 (21.9)	38.6 (9.3)	66.9[a] (–)	48.2 (7.2)	48.7[a] (–)	21.0 (15.7)
	90d	101.5 (19.7)	34.0 (5.5)	81.8 (22.2)	39.7 (5.2)	45.8 (20.6)	5.2 (4.5)
LC^3-35	14d	Undefined	104.6 (12.2)	67.7 (16.5)	81.7 (23.7)	53.4 (15.8)	74.9 (19.4)
	28d	85.5 (14.3)	104.9 (11.1)	75.8 (16.5)	73.5 (11.8)	56.2 (14.0)	67.0 (9.1)
	60d	97.7[a] (–)	97.1 (12.2)	63.9 (16.5)	80.8 (16.3)	42.7 (8.7)	46.2 (30.8)
	90d	118.3 (9.0)	72.9 (33.8)	Undefined	74.5 (24.6)	49.2 (28.7)	23.1 (15.4)
LC^3-25	14d	88.7[a] (–)	88.9 (16.0)	62.1 (14.2)	71.0 (11.9)	39.9 (8.5)	57.4 (10.7)
	28d	Undefined	88.2 (19.6)	71.9 (12.4)	81.7 (17.1)	43.8 (19.7)	62.3 (14.0)
	60d	108.2[a] (–)	101.4 (15.6)	62.4 (29.2)	90.4 (15.6)	39.7 (16.3)	62.0 (16.6)
	90d	100.3 (14.0)	103.9 (17.2)	86.8 (20.7)	114.1[a] (–)	30.1 (19.6)	72.8[a] (–)

[a] The mean values for specific metrics have limited reliability due to the limited samples (only one to three) exhibiting a given failure case.

Elucidating the mechanisms and implications of this phenomenon warrants further investigation but lies beyond the scope of the present work.

4.4. Uniaxial tensile tests

The strain-hardening response of the investigated composites is shown in Fig. 11. At 14 days, the *NC* LC^3-50-PET specimens exhibited a distinct strain-hardening response following the onset of the first crack (matrix tensile strength). By 28 days, mechanical performance metrics, such as first-crack stress, ultimate tensile strength, and strain capacity, all declined moderately relative to 14 days. With further curing, performance nearly completely diminished due to progressive PET degradation in the LC^3-50 matrix. This age-dependent loss aligns with the fiber-matrix bond loss reported over time in Section 4.3. Since attaining strain-hardening behavior requires that the fiber-bridging capacity exceed the matrix cracking strength [92,93], the concurrent loss of PET diameter and tensile capacity due to severe alkaline hydrolysis eliminated this disparity, thereby worsening *NC* LC^3-50-PET performance at later ages.

The gradual decline in the matrix tensile strength (i.e., first-crack stress) in LC^3-50 is also linked to PET degradation. The formation of surface pits and the associated reduction in diameter create dispersed defects (voids) that increase local porosity along the fiber pathways within the matrix. Due to the random distribution of fibers within the matrix, these defects are also system-wide, facilitating the early formation of microcracks due to local stress concentrations, thereby leading to matrix failure at lower stress levels [94].

In contrast, the carbonated LC^3-50-PET specimens maintained stable first-crack stress, tensile strength, and strain capacity at all curing ages. This demonstrates that enforced carbonation effectively lowers matrix alkalinity, thereby preserving the integrity of PET fibers. However, strain hardening remained limited, with typically only 1-3 cracks forming (see Appendix E, Fig. E1). Post-test fracture analysis of the 90-day specimens (Fig. 12) revealed a heterogeneous fracture structure: a carbonated outer shell in which PET fibers remained intact, and a non-carbonated core in which fibers were strongly degraded and scarcely visible. This pronounced spatial inhomogeneity likely contributed to the restricted strain hardening at later ages. Notably, a similar suppression of strain hardening was also observed at early ages (14 and 28 days), despite less significant PET degradation and favorable fiber-matrix bonding. This unexpected response is also linked to the coexistence of two competing zones within a single specimen. In the *NC* core, continued hydration produced a denser, stronger matrix (compression test results), while the fibers showed a greater tendency toward rupture (fiber/matrix bond results) and, over time, degradation. In the *C* shell, the matrix is weaker, but the fibers remained intact and tend to fail predominantly by debonding and pull-out. Hence, cracks can initiate more readily in the weaker *C* shell, but their propagation and multiplication are impeded by the stronger, denser *NC* core, thereby limiting pseudo-ductile behavior.

The tensile responses of the LC^3-35-PET composites from both the *C* and *NC* series exhibited comparable outcomes at 14 and 28 days. Beyond this age, only the *NC* specimens degraded, reflecting PET deterioration; however, the decline was substantially milder than in *NC* LC^3-50-PET at 60 and 90 days, consistent with the lower intrinsic alkalinity of the LC^3-35 matrix. The performance of the *C* LC^3-35-PET was stable across all age groups, thereby demonstrating the efficacy of carbonation in protecting alkali-sensitive fibers. Relative to *C* LC^3-50-PET, the *C* LC^3-35-PET mixtures exhibited markedly better strain hardening response at all ages – more extensive multiple cracking (*cf.* Fig. E1), higher strain capacity, and adequate matrix/composite strengths. This outcome is attributable to deeper CO_2 ingress (*cf.* Fig. 5b), which preserved PET over a larger portion of the cross-section and left only a minimal *NC* core, thereby reducing the gap between the constituents' *C/NC* properties within the specimen. Even within the residual *NC* core, slower PET degradation further narrowed the disparity in crack-bridging capacity between zones, in sharp contrast to the pronounced differentials observed in *C* LC^3-50-PET counterparts. A representative 90-day *C* LC^3-35-PET specimen illustrating these features is shown in Fig. 13.

The *NC* LC^3-25-PET composites demonstrated consistent strain-hardening performance across all curing ages under accelerated steam chamber conditions, with no indications of PET degradation or, in general, any decline in the mechanical response of the composites. This stability is attributed to the matrix's inherently low alkalinity, which is achieved by replacing 75 wt% of PC with limestone, calcined clay, and gypsum. The slight decrease in performance at 28 days is more plausibly attributed to fabrication variability than to fiber deterioration. These outcomes demonstrate that reducing the clinker content to lower matrix alkalinity is sufficient to produce PET-reinforced SHCC without CO_2 curing. This constitutes a noteworthy advancement, offering a durable, simpler, lower-carbon pathway that balances performance and sustainability while avoiding the need for additional complex treatments.

On the other hand, the fully carbonated *C* LC^3-25-PET composites also exhibited strain-hardening behavior with remarkable ductility and extensive multiple cracking. However, their matrix tensile strength and overall composite strength were consistently lower than those of their *NC* counterparts at all curing ages, as a consequence of the less dense microstructure and diminished fiber-matrix bond strength due to carbonation (as discussed in Sections 4.2 and 4.3, respectively). A visual comparison in Fig. 14 supports this explanation: the fractured surfaces of *C* LC^3-25-PET showed dusty disintegrated material, whereas their *NC* counterpart retained intact fiber-matrix integrity even to the naked eye. The observations indicate that, in highly diluted cementitious blends,

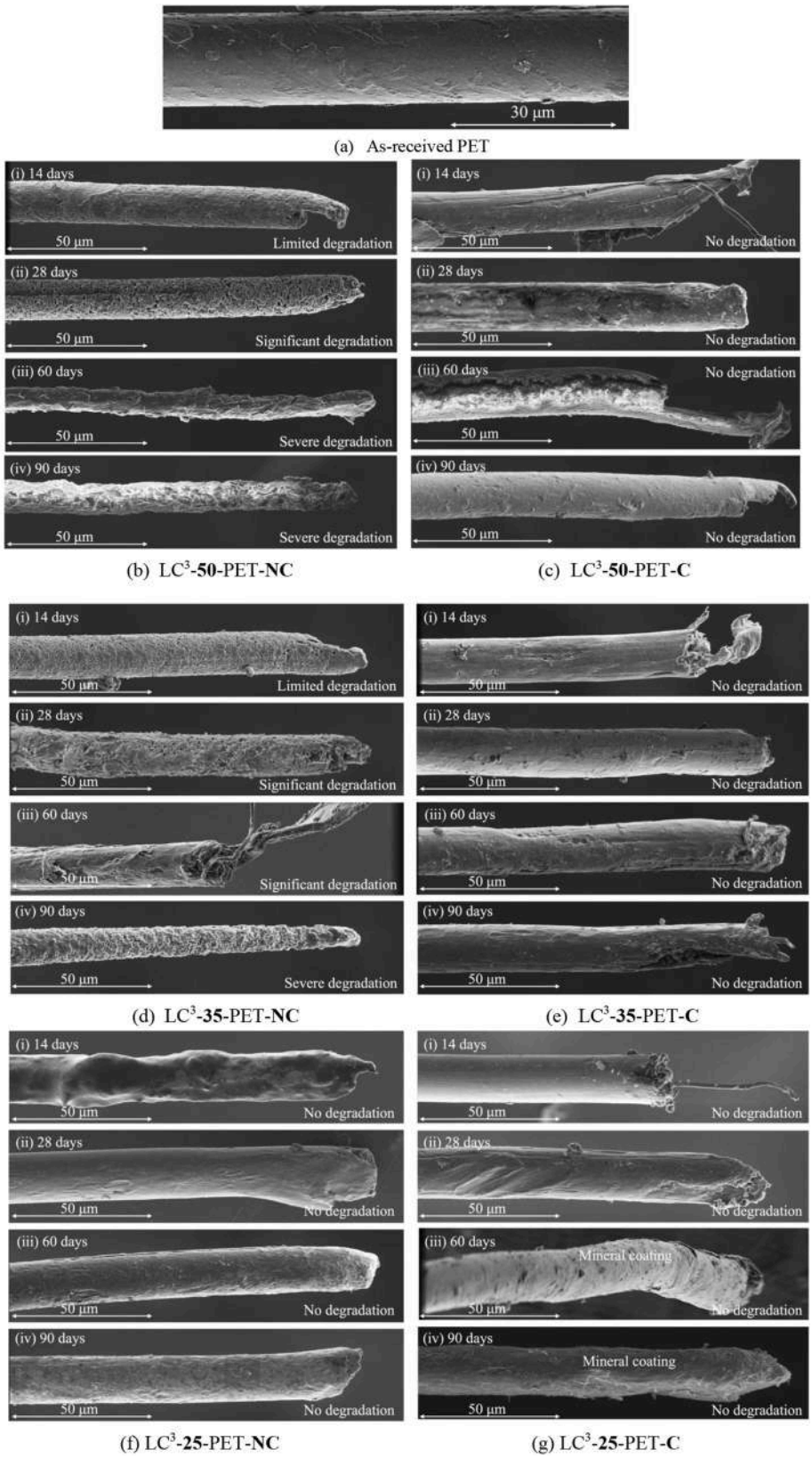

Fig. 10. SEM micrographs of as-received PET fibers **(a)** and pulled-out fibers from each fiber-matrix combination in the *C* and *NC* series at different curing ages **(b–g)**.

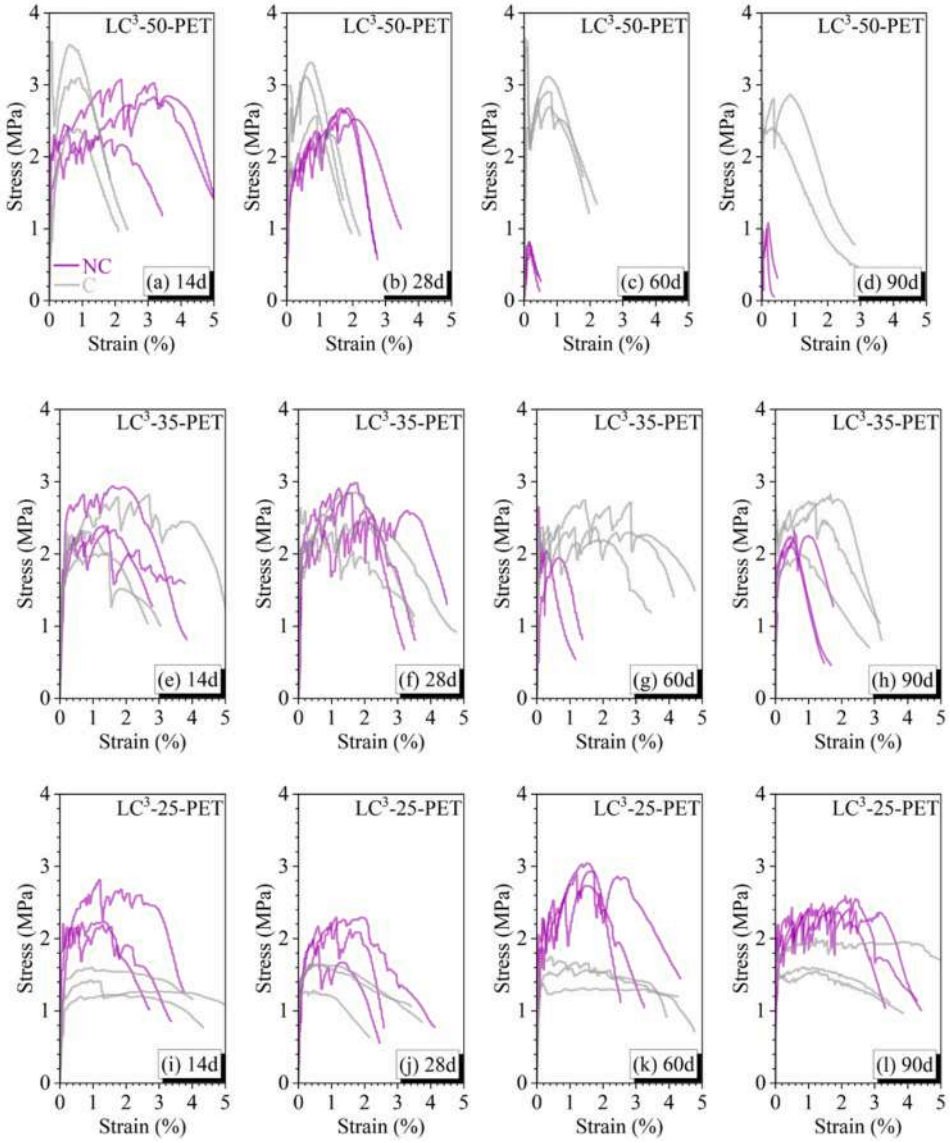

Fig. 11. Tensile stress-strain behavior of PET-reinforced SHCC with (*C*) and without (*NC*) prior carbonation curing assessed after 14, 28, 60, and 90 days of steam curing: **(a–d)** LC^3-50 matrix, **(e–h)** LC^3-35 matrix, and **(i–l)** LC^3-25 matrix.

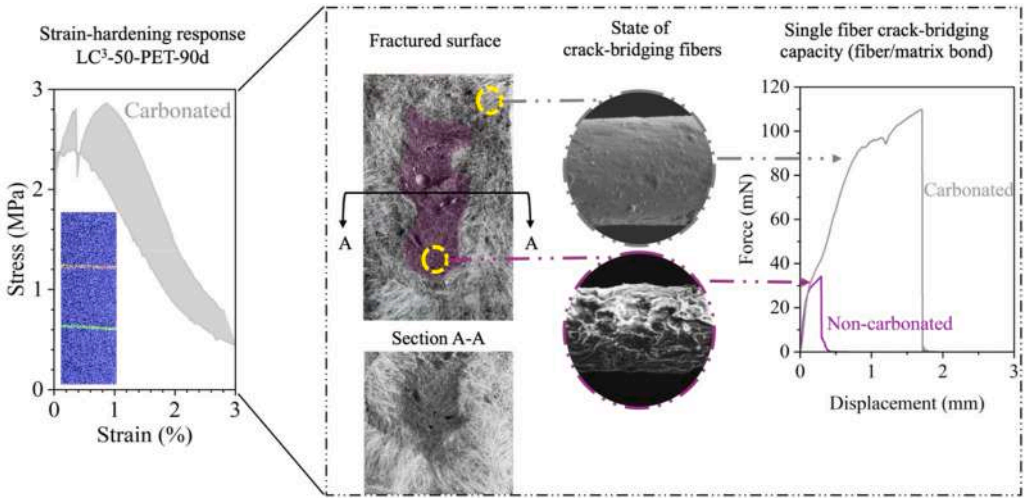

Fig. 12. *C* LC^3-50-PET specimen cured for 90 days, showing incomplete carbonation with severe PET degradation in the *NC* core and preserved PET in the *C* periphery, explaining the limited strain-hardening response.

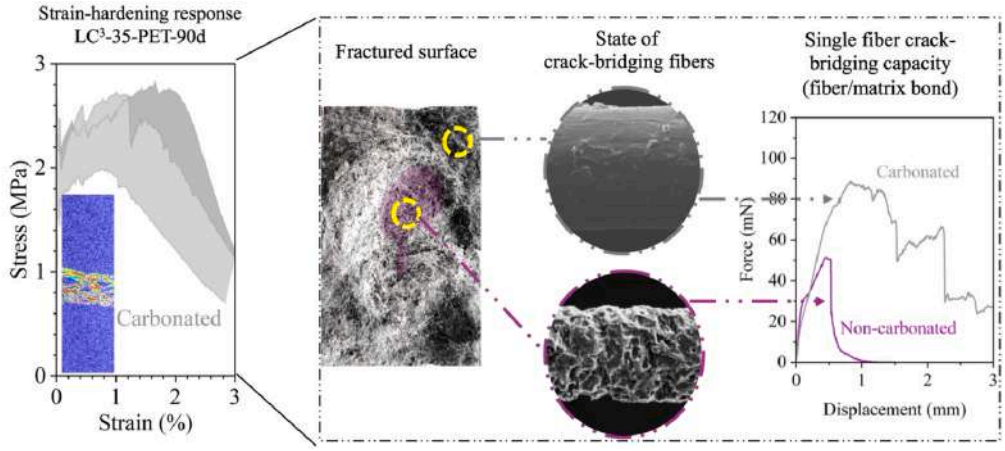

Fig. 13. *C* LC^3-35-PET specimen cured for 90 days, showing near-complete carbonation with only a minimal *NC* core. This extensive carbonation preserved most PET fibers across the cross-section, thereby sustaining their crack-bridging capacity and enabling a pronounced strain-hardening response.

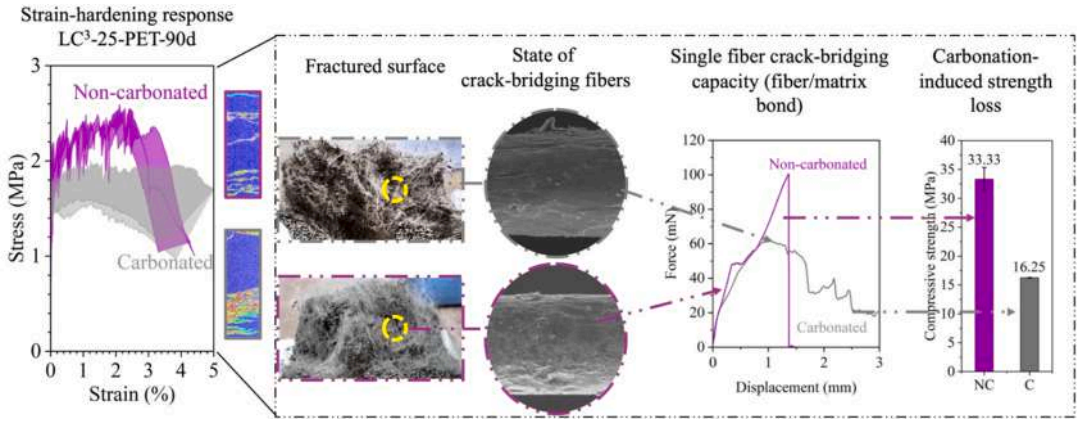

Fig. 14. *C* and *NC* LC^3-25-PET specimens cured for 90 days. The fractured surface of *C* specimens exhibits a less-dense microstructure and reduced fiber crack-bridging capacity compared to the *NC* specimens due to carbonation-induced strength loss in the LC^3-25 matrix, which underpins the observed strain-hardening response.

carbonation reduces microstructural densification and generates additional matrix defects, thereby weakening the matrix. This, in turn, fosters easier crack initiation and propagation due to diminished matrix fracture toughness (*cf*. the crack patterns in Fig. E1). However, the weakened fiber-matrix bond constrained the crack-bridging capacity of PET fibers, resulting in a flat or even negative slope in the strain-hardening phase. Consequently, in these composites, the ultimate strain capacity is not defined relative to the ultimate tensile strength, but rather at the point where the slope of the strain-hardening phase deviates markedly from the general trend. This deviation marks the termination of multiple cracking and the onset of softening through localized crack opening.

This comparison underscores a practical issue: the *NC* LC^3-25-PET system doesn't promote PET degradation due to its inherently lower alkalinity and demonstrates superior performance compared to the *C* variant, which shows significant matrix weakening from carbonation. However, in practice, LC^3-25-PET can naturally carbonate during service, potentially leading to deterioration in mechanical performance, akin to that of *C* LC^3-25-PET. Consequently, this risk should be considered when selecting LC^3 formulations for PET-reinforced SHCC. Perhaps LC^3-50 and LC^3-35 may be more suitable candidates under fully carbonated conditions, as the associated reduction in microstructural densification is expected to be less severe, thereby supporting improved strain-hardening behavior. Future investigations will assess this hypothesis by fully carbonating these matrices with PET fibers inside.

Fig. 15 offers a comprehensive overview of the key mechanical performance metrics derived from uniaxial tensile tests. The findings demonstrate that all matrices exhibited an anti-aging response; however, the retention of tensile properties was critically dependent on the integrity of PET fibers. Specifically, in all matrices within the *C* series and the only *NC* series matrix, LC^3-25-PET – where PET degradation was absent – parameters such as first crack stress (Fig. 15 (a)), tensile strength (Fig. 15 (b)), and tensile strain capacity (Fig. 15 (d)) remained stable against aging. In contrast, in *NC* LC^3-50-PET and *NC* LC^3-35-PET, PET degradation increasingly undermined crack-bridging capacity, resulting in a progressive reduction in tensile properties and, at advanced stages, a loss of strain capacity.

With respect to crack-width control (Fig. 15 (e)), most composites maintained crack widths within 150–250 μm, even in cases where severe PET degradation occurred at later ages in *NC* LC^3-50-PET and *NC* LC^3-35-PET. This range, as expected, is relatively high compared to typically reported data for SHCC, where crack widths are around ~50 μm for PVA-based systems [13] and ~100 μm for PE-based systems [95]. The larger crack widths in PET-reinforced composites are attributed to the intrinsically weaker bond between PET fibers and cementitious matrices, combined with the low Young's modulus of PET fibers. As a "large rupture strain" fiber [96], PET undergoes substantial plastic deformation before failure (as can be seen in Fig. 9), which reduces its efficiency in tightly controlling crack widths. However, in specialized applications such as impact loading, the energy absorption resulting

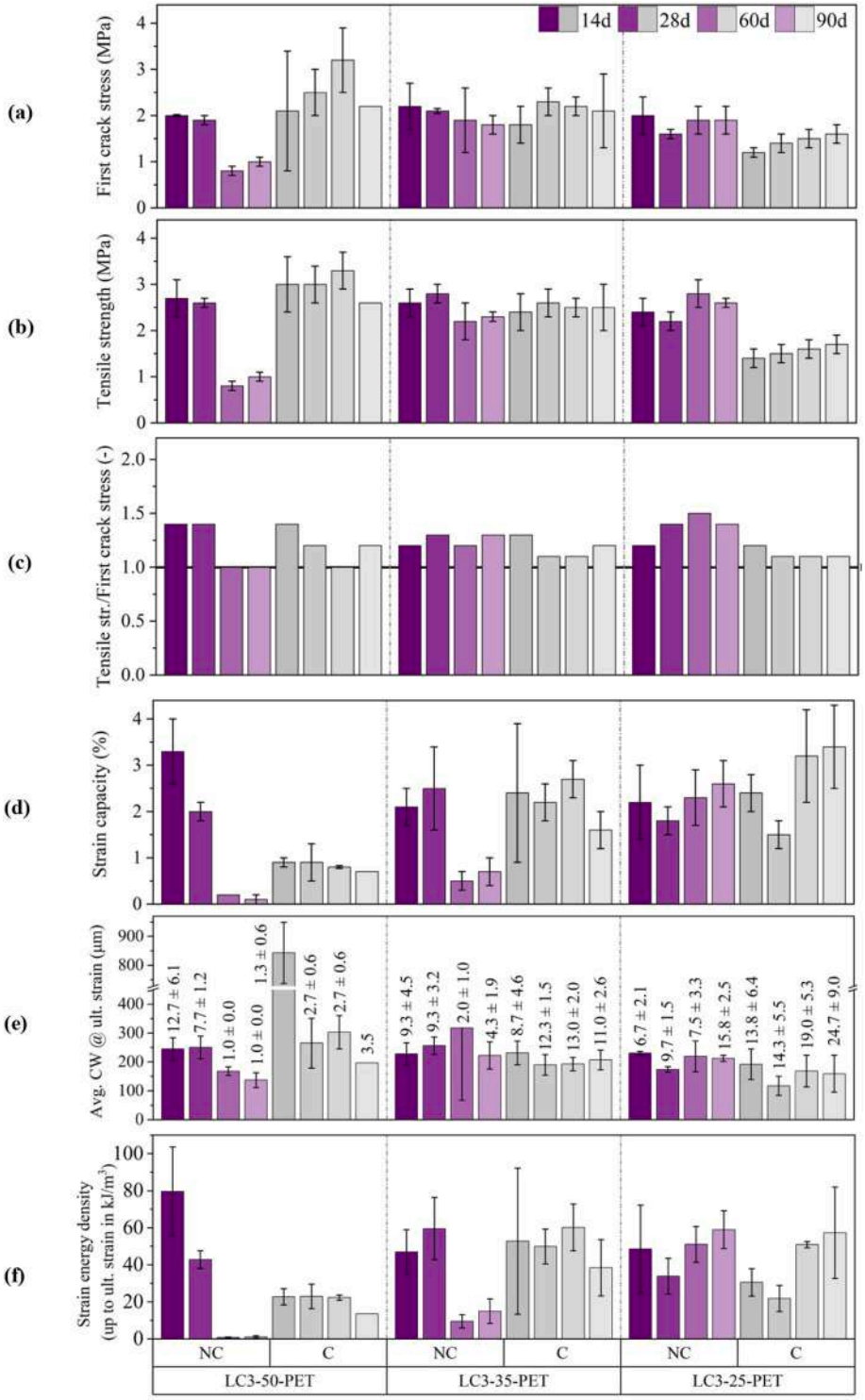

Fig. 15. Summary of key mechanical parameters from the tensile stress-strain behavior of PET-reinforced SHCC after 14, 28, 60, and 90 days of steam curing, with and without prior carbonation: **(a)** first-crack stress, **(b)** composite tensile strength, **(c)** ratio of tensile strength to first crack stress, **(d)** strain capacity, **(e)** average crack width at ultimate strain with corresponding crack density (per 100 mm gauge length), and **(f)** strain energy density up to ultimate strain.

from wider cracking is deemed acceptable. This is particularly relevant in damping protective layers, where high compliance can be advantageous. In such contexts, these specialized formulations could serve as optimal and sustainable alternatives [19].

A notable exception to the overall trend in crack width was seen in *C*LC^3-50-PET, especially at 14 days, where it displayed unusually wide cracks (800-900 μm). This anomaly is not fully understood, but it is likely related to incomplete carbonation, resulting in coexisting *C/NC* zones within the same specimen. These zones exhibited markedly different responses due to carbonation-induced matrix alterations and the contrasting crack-bridging response of PET fibers.

Fig. 15 (c) presents the ratio of composite tensile strength to first-crack stress as an indicator of the robustness of the strain-hardening behavior. A ratio greater than 1 indicates that the peak fiber-bridging capacity exceeds the matrix cracking strength, enabling stable multiple cracking and strain hardening [92,93,97,98]; values close to 1

suggest limited multiple cracking, while ratios below 1 are characteristic of strain-softening FRC. As shown in Fig. 15 (c), *NC* LC^3-50-PET exhibited ratios greater than 1 at early ages, consistent with the high crack density marked in Fig. 15 (e) and visually represented in the DIC crack patterns in Fig. E1. Similarly, *NC* LC^3-35-PET and *NC* LC^3-25-PET exhibited ratios greater than 1, corresponding to distributed multiple cracking. However, when PET fibers underwent severe degradation, their crack-bridging capacity was compromised. This is evident for *NC* LC^3-50-PET at 60 and 90 days, where only a single crack formed, and the ratio approached 1. A similar trend was observed at later ages for *NC* LC^3-35-PET, where the ratio began to decrease, accompanied by a reduction in crack density. An exception was observed for *C* LC^3-25-PET, where the ratio remained only slightly above 1 despite the presence of highly saturated multiple cracking. This behavior is attributed to carbonation-induced reductions in matrix strength and fracture toughness, which facilitate crack initiation, while the relatively low fiber-bridging capacity across cracks explains the nearly flat or slightly negative slope of the strain-hardening phase discussed earlier.

Finally, Fig. 15 (f) presents the strain energy density up to the ultimate strain. Specimens subjected to PET degradation exhibited markedly lower strain energy density, with reductions closely aligned with the extent of fiber deterioration. Conversely, composites in which PET fibers remained intact consistently demonstrated significantly higher strain energy density across all curing periods. This parameter is particularly significant for impact- and earthquake-resistant structures, as elevated strain energy density indicates an enhanced capacity to dissipate tensile energy prior to failure, facilitated by stable multiple cracking due to adequate fiber bridging capacity [17].

Preserving PET fiber integrity – whether through low-clinker matrix formulations or enforced carbonation curing – effectively maintains interfacial stress transfer and crack-bridging capabilities, thereby sustaining adequate strain energy density. A noteworthy example is *C* LC^3-25-PET. While carbonation may reduce matrix strength and weaken the fiber-matrix interface, it can also induce more extensive multiple cracking, thereby increasing the tensile strain capacity. As a result, the decrease in tensile strength is counterbalanced by increased deformability, yielding strain energy density values comparable to those of *NC* counterparts.

From an application standpoint, these findings indicate that the low-clinker LC^3-25-PET composite may continue to serve effectively as a thin strengthening layer for existing structures for protection against dynamic loading conditions, even after natural carbonation, as its key functional property – energy dissipation – remains intact. Nonetheless, this hypothesis necessitates direct validation through dynamic testing of both *C* and *NC* LC^3-25-PET composites.

5. Summary and conclusions

In this study, a series of LC^3-based PET-reinforced SHCC were designed and subjected to accelerated steam curing for 14, 28, 60, and 90 days, with (*C*) and without (*NC*) prior enforced carbonation curing. The overarching objective was to mitigate alkaline degradation of PET fibers, as they are highly susceptible to alkaline hydrolysis when embedded in cementitious matrices, thereby sustaining the mechanical and durability performance of the composites. At each curing age, carbonation depth was quantified, and the composites were systematically evaluated through mechanical testing. The experimental program included compressive strength measurements, single fiber-matrix bond assessments, and uniaxial tensile testing to capture strain-hardening behavior, complemented by optical microscopy and ESEM imaging for microstructural investigations.

The following conclusions can be drawn:

- The severity and kinetics of PET degradation depend on matrix alkalinity, governed by PC content. In the high-clinker LC^3-50 matrix, elevated alkalinity accelerated degradation after 60 days of steam curing. Reducing PC replacement to 65 wt% (LC^3-35) decreased alkalinity and slowed degradation, while at 75 wt% (LC^3-25), alkalinity was low enough to prevent PET degradation.
- PET degradation manifested as surface pitting, reduction in fiber diameter, and loss of load-bearing capacity. These deterioration mechanisms weakened the fiber-matrix interfacial bond, reducing crack-bridging capacity and ultimately suppressing strain-hardening behavior in SHCC. Consequently, highly alkaline *NC* LC^3-50-PET and *NC* LC^3-35-PET showed progressive loss of strain-hardening at later ages, whereas low-alkalinity *NC* LC^3-25-PET retained stable tensile behavior.
- Carbonation curing effectively inhibited PET degradation across all matrices by lowering alkalinity and preserving fiber integrity.
- Carbonation penetration depth was composition-dependent: the dense LC^3-50 matrix limited CO_2 diffusion, whereas the more porous LC^3-35 and LC^3-25 matrices allowed deeper ingress.
- In highly diluted blends, carbonation induced microstructural loosening, reducing matrix strength and fiber-matrix bond. These effects increased with the level of PC replacement. As a result, in LC^3-25, carbonation was unnecessary and even detrimental, as PET fibers were already stable in the low-alkalinity matrix, and additional carbonation impaired the strain-hardening performance.
- Both *C* and *NC* LC^3 matrices exhibited an anti-aging response under steam curing, stabilizing compressive and tensile strength as long as PET fibers remained preserved, a valuable trait for SHCC, where ongoing hydration often reduces strain capacity.

In essence, carbonation transforms higher-clinker LC^3 systems from environmentally unsustainable, PET fiber-degrading matrices into durable, CO_2-sequestering composites that preserve mechanical performance. In contrast, in low-clinker, SCM-rich systems such as LC^3-25, which are inherently environmentally sustainable, carbonation becomes counterproductive, reducing mechanical performance. These findings highlight the need for composition-specific design strategies: carbonation curing is effective as a sustainability and durability tool in high-clinker systems, while low-clinker matrices rely on their inherently low alkalinity to safeguard alkali-sensitive fibers like PET.

6. Future directions

As this study is a pioneering exploration of the carbonation process in highly diluted LC^3-based SHCC reinforced with alkali-sensitive PET fibers, it opens several avenues for future research exploration:

- Optimize composition-dependent carbonation protocols to ensure full carbonation across various LC^3 matrices, especially LC^3-50, which was only partially carbonated under the current conditions.
- Verify the microstructural evolution caused by carbonation and measure CO_2 uptake in LC^3 binders with systematically varied clinker contents, employing advanced characterization methods such as QXRD, TGA/DTG, MIP, ESEM-EDX, and FTIR.
- Develop a predictive model of PET degradation by investigating fiber behavior in controlled-pore solution chemistries (varying pH) that replicate LC^3 environments.
- Conduct a comprehensive life cycle assessment (LCA) to evaluate the environmental and economic impacts of integrating carbonation curing into LC^3-based SHCC with PET fibers and establish its role as a pathway toward sustainable and durable composites.

CRediT authorship contribution statement

Ameer Hamza Ahmed: Writing – review & editing, Writing – original draft, Visualization, Methodology, Investigation, Formal analysis, Data curation, Conceptualization. **Anna Jose:** Writing – review & editing, Writing – original draft, Validation, Investigation, Formal analysis, Data curation. **Cesare Signorini:** Writing – review & editing,

Visualization, Validation, Supervision. **Marco Liebscher:** Writing – review & editing, Visualization, Validation, Supervision, Project administration, Funding acquisition. **Marko Butler:** Writing – review & editing, Visualization, Validation, Supervision. **Viktor Mechtcherine:** Writing – review & editing, Validation, Supervision, Resources, Project administration, Funding acquisition.

Funding

This work was supported by the Deutsche Forschungsgemeinschaft (DFG, German Research Foundation) within the Research Training Group GRK 2250/3, titled "Mineral-bonded composites for enhanced structural impact safety" (project 287321140), and through Germany's Excellence Strategy – EXC 3115 – 533767731.

Declaration of competing interest

The authors declare that they have no known competing financial interests or personal relationships that could have appeared to influence the work reported in this paper.

Appendix A

In this appendix, chemical, mineralogical, and physical properties of binder constituents in LC^3-based mixtures are listed.

Table A1
Chemical composition (wt.%) of the raw binder ingredients as determined by energy dispersive X-ray (EDX) analysis.

Chemical oxides	Portland cement	Calcined clay	Limestone	Gypsum
SiO_2	15.9	47.4	7.3	0.9
Al_2O_3	4.1	24.8	1.9	3.3
Fe_2O_3	2.8	8.9	0.8	0.1
CaO	71.2	8.6	75.4	43.2
MgO	0.7	2.8	14.1	1.1
SO_3	4.0	2.2	-	51.1
P_2O_5	-	-	0.2	0.1
K_2O	0.4	3.6	0.4	0.1
Na_2O	0.6	0.4	0.5	-
TiO_2	-	1.3	-	-

Table A2
The mineral composition of raw binder materials determined by XRD-Rietveld analysis.

Portland cement		Calcined clay		Limestone		Gypsum	
Minerals	Wt. [%]	Minerals	Wt. [%]	Minerals	Wt. [%]	Minerals	Wt. [%]
C_3S	54	Quartz	18.8	Calcite	54	Gypsum	91
C_2S	20	Mica	6.6	Dolomite	44	Anhydrite	6
C_3A	7	Feldspar	4.9	Others	2	Calcite	3
C_4AF	9	Anhydrite	1.8	-	-	-	-
Calcite	5	Calcite	1.8	-	-	-	-
Gypsum	2	C_3A	0.4	-	-	-	-
Bassanite	3	Amorphous	65.7	-	-	-	-

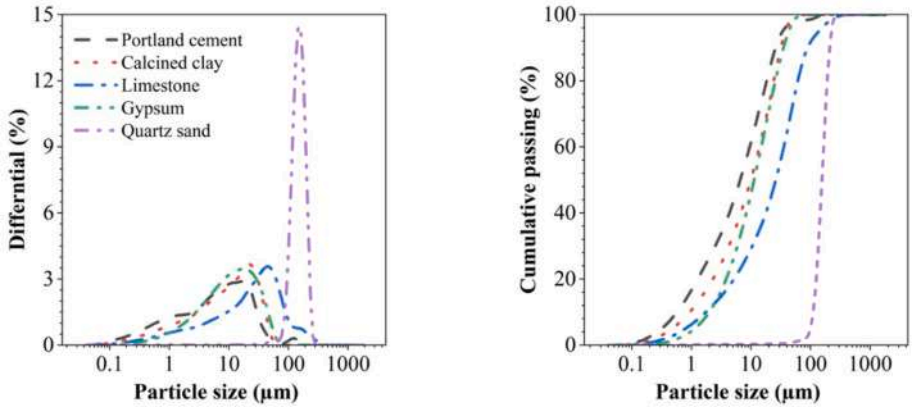

Fig. A1. Particle size distribution of raw ingredients.

Appendix B

This appendix presents images of prismatic cross-sections (40 × 40 mm^2) of *NC* and *C* samples, utilizing phenolphthalein indicators for LC^3-50, LC^3-35, and LC^3-25 mortars (free of fibers).

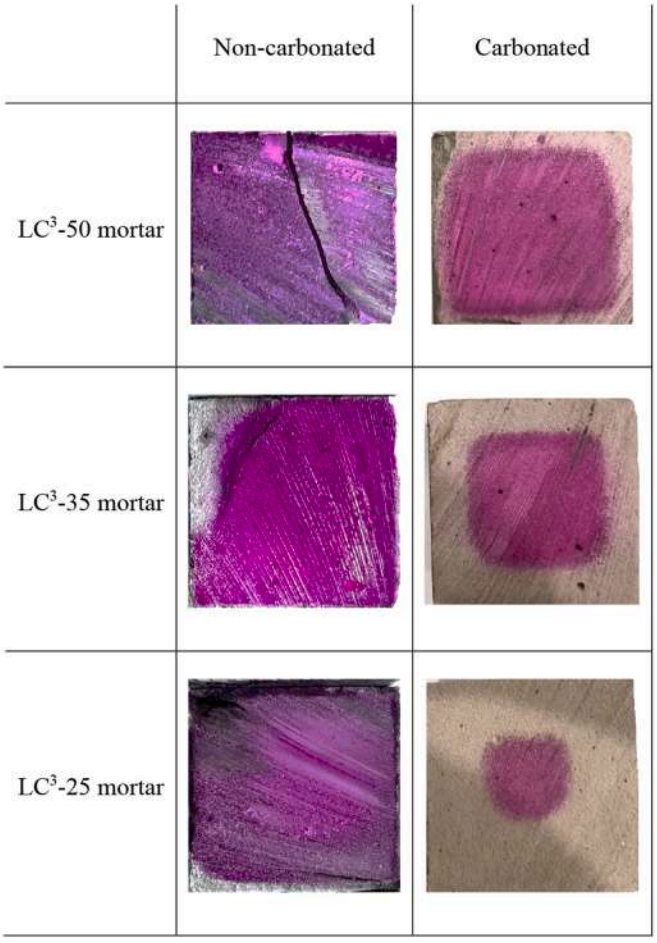

Fig. B1. Prismatic cross-sections of LC^3-50, LC^3-35, and LC^3-25 mortars (fiber-free), with phenolphthalein indicators showing carbonation depth and the shape of the carbon dioxide front.

Appendix C

In this appendix, the compression strength data are presented in tabular form.

Table C1
Average compressive strength of LC^3-PET composites with (*C*) and without (*NC*) enforced carbonation, cured in a steam chamber at various ages. Values in parentheses represent the standard deviation. The percentage decrease (% dec.) is calculated relative to *NC* LC^3-50-PET to highlight the effect of mixture composition and prior carbonation on compressive strength.

	LC^3-50-PET			LC^3-35-PET				LC^3-25-PET			
	NC (Ref)	*C*	*% Dec.*	*NC*	*% Dec.*	*C*	*% Dec.*	*NC*	*% Dec.*	*C*	*% Dec.*
14d	47.7 (5.4)	44.7 (2.8)	6.3	41.2 (1.8)	13.6	30.7 (2.7)	35.6	33.9 (3.2)	28.9	16.0 (1.9)	66.5
28d	53.6 (2.5)	46.9 (1.6)	12.5	40.6 (1.8)	24.2	31.5 (0.8)	41.2	33.6 (2.6)	37.3	16.2 (2.6)	69.8
60d	45.2 (3.9)	44.3 (2.3)	2.0	40.8 (1.0)	9.7	26.3 (1.1)	41.8	34.0 (1.6)	24.8	16.3 (0.6)	64.0
90d	51.9 (1.7)	45.0 (3.9)	13.3	42.2 (3.8)	18.7	31.2 (2.3)	39.9	33.3 (2.0)	35.8	16.3 (0.1)	68.6

Appendix D

In this appendix, the force *vs.* displacement curves from all single fiber pull-out tests are presented.

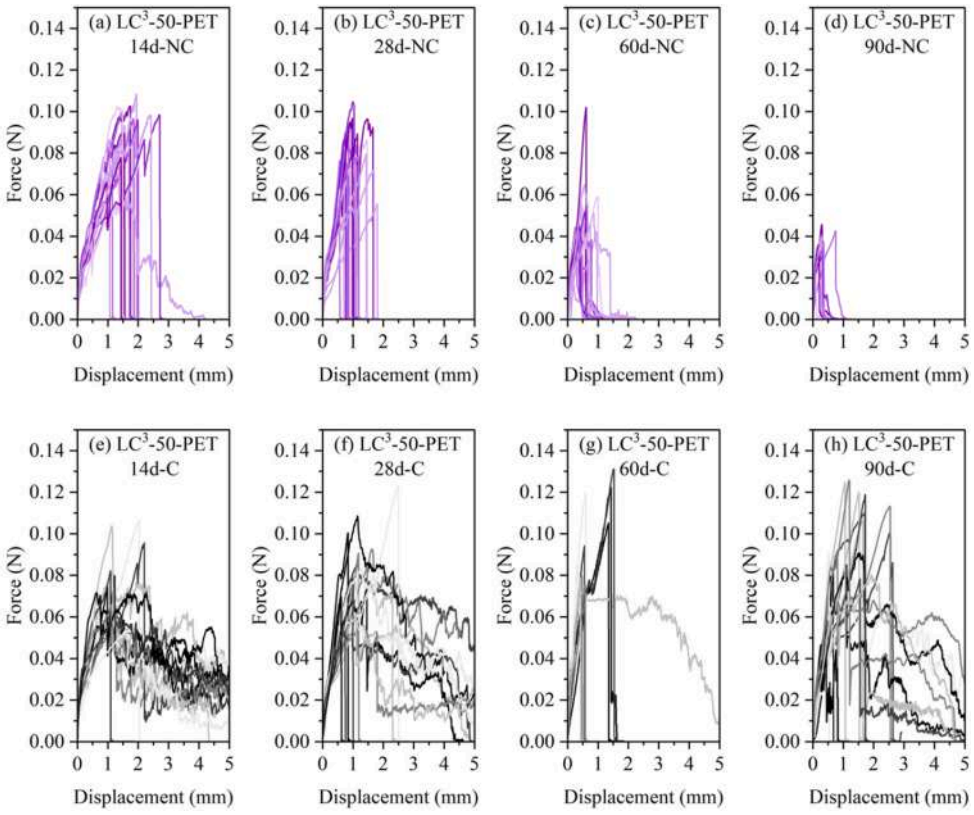

Fig. D1. Single fiber pullout response of PET fibers from LC^3-50 matrix after 14, 28, 60, and 90 days of steam curing: **(a–d)** without pre-curing carbonation (*NC*), and **(e–h)** with pre-curing carbonation (*C*).

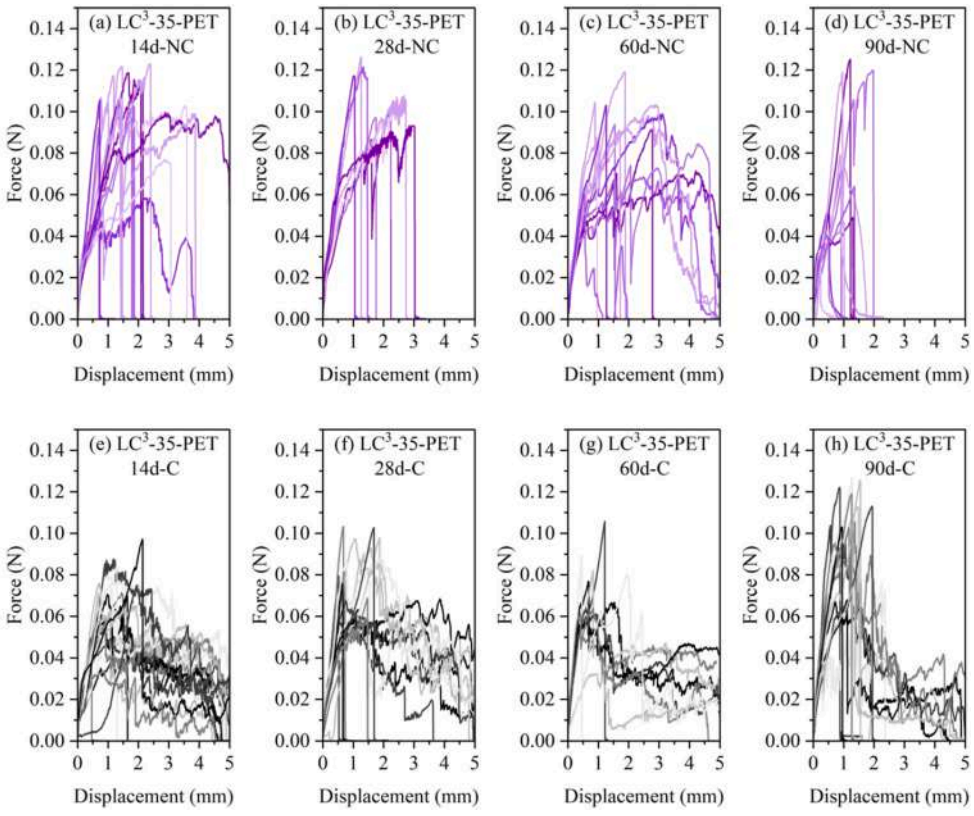

Fig. D2. Single fiber pullout response of PET fibers from LC^3-35 matrix after 14, 28, 60, and 90 days of steam curing: **(a–d)** without pre-curing carbonation (*NC*), and **(e–h)** with pre-curing carbonation (*C*).

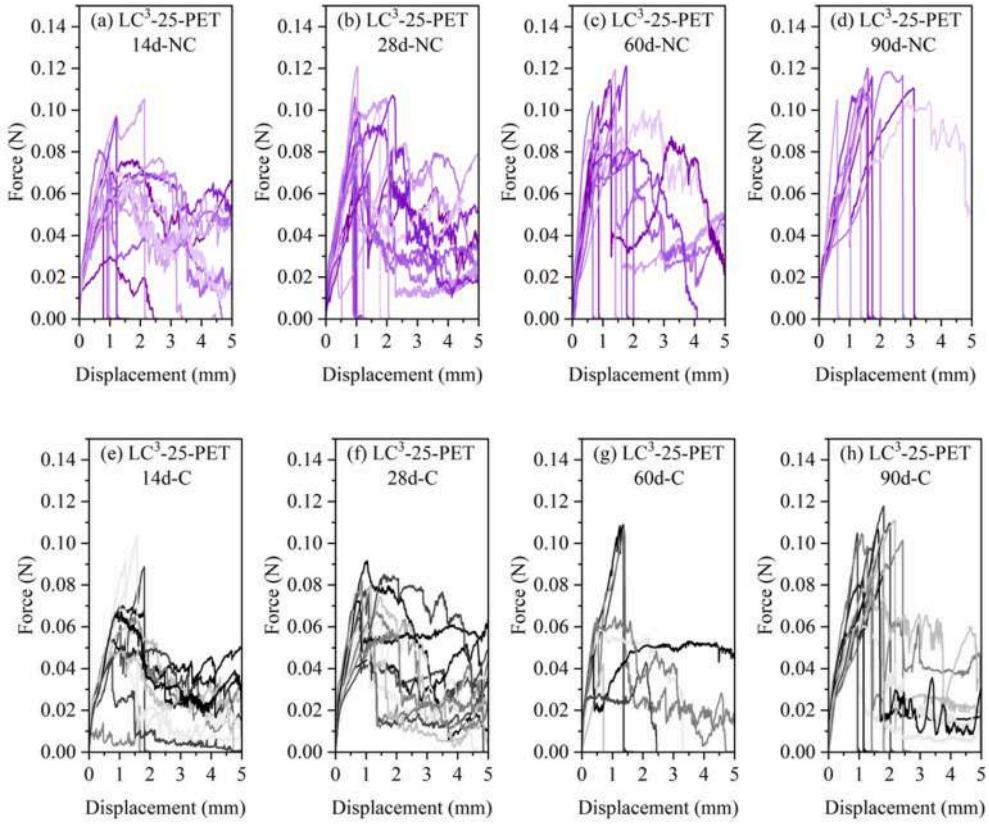

Fig. D3. Single fiber pullout response of PET fibers from LC^3-25 matrix after 14, 28, 60, and 90 days of steam curing: **(a–d)** without pre-curing carbonation (*NC*), and **(e–h)** with pre-curing carbonation (*C*).

Appendix E

In this appendix, the DIC crack pattern at ultimate strain is presented.

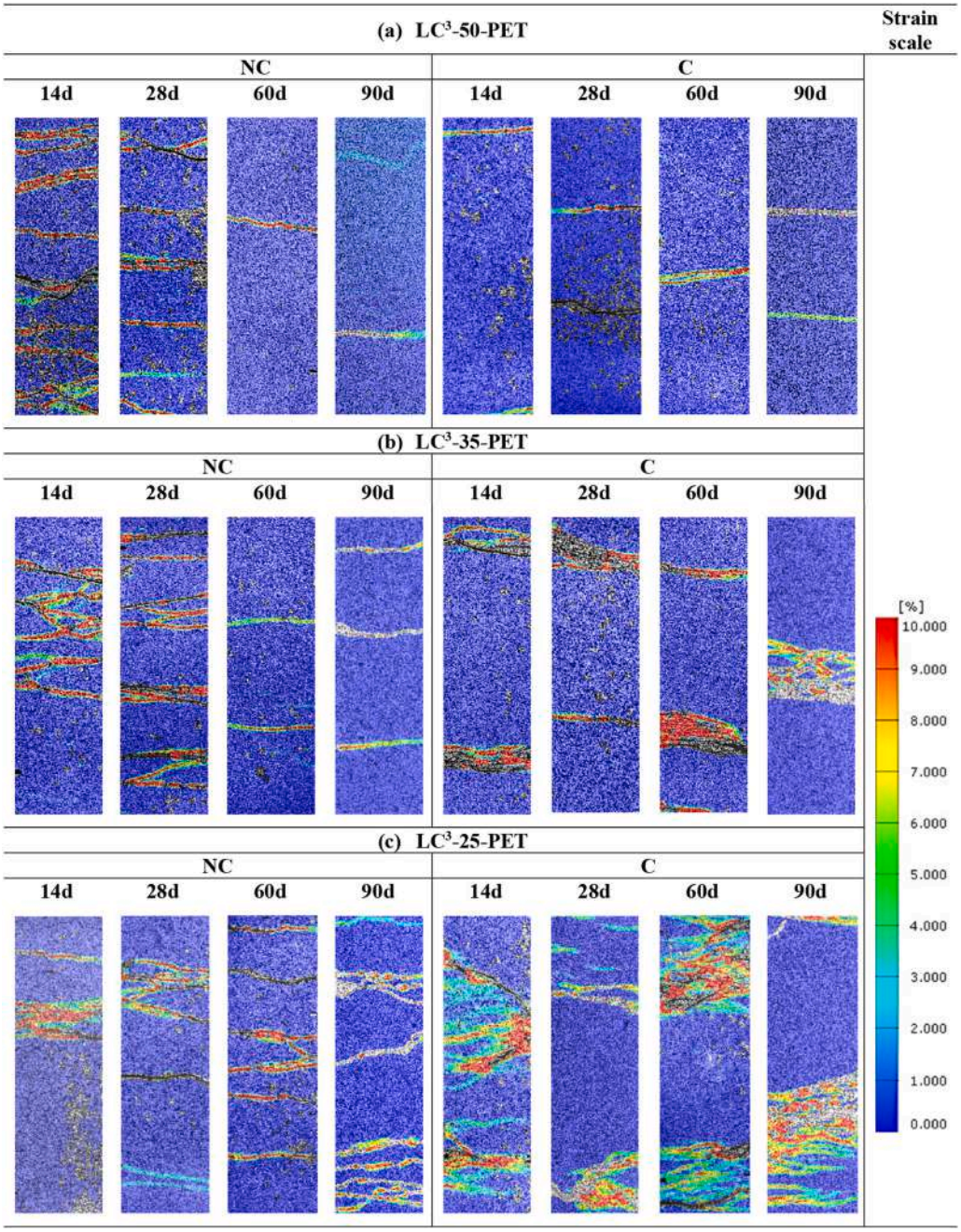

Fig. E1. DIC-derived crack patterns of the investigated composites subjected to accelerated steam curing for 14, 28, 60, and 90 days: (a) LC^3-50-PET, (b) LC^3-35-PET, and (c) LC^3-25-PET, with (*C*) and without (*NC*) prior carbonation curing.

Data availability

Data will be made available on request.

References

[1] V.C. Li, On engineered cementitious composites (ECC), J. Adv. Concr. Technol. 1 (2003) 215–230, https://doi.org/10.3151/jact.1.215.

[2] E.-H. Yang, Y. Yang, V. Li, Use of high volumes of fly ash to improve ECC mechanical properties and material greenness, ACI Mater. J. 104 (2007) 620–628, https://doi.org/10.14359/18966.

[3] A.E. Naaman, H.W. Reinhardt (Eds.), High Performance Fiber Reinforced Cement Composites 2: Proceedings of the Second International RILEM Workshop, CRC Press, London, 1996, https://doi.org/10.1201/9781482271676.

[4] L.-Y. Xu, J.-C. Lao, D.-D. Shi, J. Cai, T.-Y. Xie, B.-T. Huang, Recent advances in high-strength engineered geopolymer composites (HS-EGC): bridging sustainable construction and resilient infrastructure, Cem. Concr. Compos. 165 (2026) 106307, https://doi.org/10.1016/j.cemconcomp.2025.106307.

[5] B.-T. Huang, H. Xi, R.-Y. Ma, Z.-L. Zhang, J.-C. Lao, H. Zhang, Y.-N. Shen, D.-D. Shi, L.-Y. Xu, Ultra-high-strength engineered geopolymer composites (UHS-EGC) with mineral processing waste: probabilistic modeling of cracking behavior, Theor. Appl. Fract. Mech. 140 (2025) 105138, https://doi.org/10.1016/j.tafmec.2025.105138.

[6] H. Xi, Z.-L. Zhang, F.-Y. Zhuo, L.-J. Hou, H. Zhang, W.-J. Zhang, X.-H. Ji, K.-C. Liu, Y.-N. Shen, J.-C. Lao, High-strength high-ductility Engineered/strain-hardening

geopolymer composites (EGC/SHGC) incorporating dredged river sand, Case Stud. Constr. Mater. 22 (2025) e04796, https://doi.org/10.1016/j.cscm.2025.e04796.
[7] V. Mechtcherine, Novel cement-based composites for the strengthening and repair of concrete structures, Constr. Build. Mater. 41 (2013) 365–373, https://doi.org/10.1016/j.conbuildmat.2012.11.117.
[8] Y.M. Lim, V.C. Li, Durable repair of aged infrastructures using trapping mechanism of engineered cementitious composites, Cem. Concr. Compos. 19 (1997) 373–385, https://doi.org/10.1016/S0958-9465(97)00026-7.
[9] S. Müller, V. Mechtcherine, Use of strain-hardening cement-based composites (SHCC) for retrofitting, MATEC Web Conf. 199 (2018) 09006, https://doi.org/10.1051/matecconf/201819909006.
[10] T.C.S.P. Figueiredo, M. Hering, I. Curosu, F. Bracklow, S. Scheerer, M. Curbach, V. Mechtcherine, F.D.A. Silva, Effect of shear reinforcement and external strengthening with strain-hardening cement-based composites (SHCC) on the impact resistance of reinforced concrete beams, Cem. Concr. Compos. 145 (2024) 105371, https://doi.org/10.1016/j.cemconcomp.2023.105371.
[11] V. Mechtcherine, I. Curosu, Mineral-bonded composites for enhanced structural impact safety – a new research training group GRK 2250 of the German research society, Procedia Eng. 210 (2017) 182–185, https://doi.org/10.1016/j.proeng.2017.11.064.
[12] Q. Liao, J.-T. Yu, F.-Y. Dong, R. Fediuk, K.-Q. Yu, Tension-shear characteristics, cost and environmental impact of polyethylene fiber reinforced engineered cementitious composites: the role of fiber content, Constr. Build. Mater. 428 (2024) 136312, https://doi.org/10.1016/j.conbuildmat.2024.136312.
[13] D. Zhang, B. Jaworska, H. Zhu, K. Dahlquist, V.C. Li, Engineered cementitious composites (ECC) with limestone calcined clay cement (LC3), Cem. Concr. Compos. 114 (2020) 103766, https://doi.org/10.1016/j.cemconcomp.2020.103766.
[14] V. Li, Engineered cementitious composites (ECC) – material, structural, and durability performance, in: Concr. Constr. Eng. Handb., second ed., CRC Press, 2008, p. 48.
[15] V.C. Li, M. Lepech, Crack Resistant Concrete Material for Transportation Construction: Proceedings of Transportation Research Board 83rd Annual Meeting, Compendium of Papers CD ROM, Washington, DC, 2004, pp. 4–4680. Paper.
[16] V. Mechtcherine, O. Millon, M. Butler, K. Thoma, Mechanical behaviour of strain hardening cement-based composites under impact loading, Cem. Concr. Compos. 33 (2011) 1–11, https://doi.org/10.1016/j.cemconcomp.2010.09.018.
[17] I. Curosu, V. Mechtcherine, D. Forni, E. Cadoni, Performance of various strain-hardening cement-based composites (SHCC) subject to uniaxial impact tensile loading, Cement Concr. Res. 102 (2017) 16–28, https://doi.org/10.1016/j.cemconres.2017.08.008.
[18] I. Curosu, V. Mechtcherine, O. Millon, Effect of fiber properties and matrix composition on the tensile behavior of strain-hardening cement-based composites (SHCCs) subject to impact loading, Cement Concr. Res. 82 (2016) 23–35, https://doi.org/10.1016/j.cemconres.2015.12.008.
[19] L. Leicht, M. Colombo, P. Martinelli, C. Signorini, V. Mechtcherine, M. di Prisco, S. Scheerer, M. Curbach, B. Beckmann, Protective potential of high-contrast mineral-bonded layers on reinforced concrete slabs subjected to uniform shock waves, Int. J. Impact Eng. 196 (2025) 105149, https://doi.org/10.1016/j.ijimpeng.2024.105149.
[20] T. Gong, A.H. Ahmed, I. Curosu, V. Mechtcherine, Tensile behavior of hybrid fiber reinforced composites made of strain-hardening cement-based composites (SHCC) and carbon textile, Constr. Build. Mater. 262 (2020) 120913, https://doi.org/10.1016/j.conbuildmat.2020.120913.
[21] L. Wang, N. Ur Rehman, I. Curosu, Z. Zhu, M.A.B. Beigh, M. Liebscher, L. Chen, D. C.W. Tsang, S. Hempel, V. Mechtcherine, On the use of limestone calcined clay cement (LC3) in high-strength strain-hardening cement-based composites (HS-SHCC), Cement Concr. Res. 144 (2021) 106421, https://doi.org/10.1016/j.cemconres.2021.106421.
[22] R. Frenzel, A. Drechsler, F. Simon, C. Zimmerer, A. Synytska, A. Bashiri Rezaie, A. H. Ahmed, M. Liebscher, V. Mechtcherine, Enhanced bonding of polyethylene fibers in strain-hardening cementitious composites through polydopamine interphase: insights from micro- and mesoscale testing, Appl. Surf. Sci. 710 (2025) 163898, https://doi.org/10.1016/j.apsusc.2025.163898.
[23] R. Frenzel, A. Drechsler, C. Zimmerer, A. Synytska, A. Bashiri Rezaie, A.H. Ahmed, M. Liebscher, V. Mechtcherine, Combined polydopamine/polyelectrolyte modification of polyethylene fibers to promote adhesion in fiber-reinforced cement composites, Colloids Surf. A Physicochem. Eng. Asp. 727 (2025) 138175, https://doi.org/10.1016/j.colsurfa.2025.138175.
[24] D. Zhang, J. Yu, H. Wu, B. Jaworska, B.R. Ellis, V.C. Li, Discontinuous micro-fibers as intrinsic reinforcement for ductile engineered cementitious composites (ECC), Composites, Part B Eng. 184 (2020) 107741, https://doi.org/10.1016/j.compositesb.2020.107741.
[25] R. Hufenus, Y. Yan, M. Dauner, T. Kikutani, Melt-spun fibers for textile applications, Materials 13 (2020) 4298, https://doi.org/10.3390/ma13194298.
[26] A.H. Ahmed, J. Hübner, D. Junger, C. Signorini, M. Butler, M. Liebscher, C. Scheffler, V. Mechtcherine, Engineering low clinker strain-hardening cementitious composites (SHCC) using polyethylene and cost-effective polypropylene fibers: an experimental scale-linking analysis, Mater. Des. 254 (2025) 114051, https://doi.org/10.1016/j.matdes.2025.114051.
[27] Textile Exchange, Preferred Fiber & Materials Market Report, (2022). https://textileexchange.org/app/uploads/2022/10/Textile-Exchange_PFMR_2022.pdf (accessed May 17, 2023).
[28] Diversified Enterprises, Critical surface tension and contact angle with water for various polymers (sort by contact angle), (n.d.). https://www.accudynetest.com/polytable_03.html?sortby=contact_angle (accessed July 1, 2024).
[29] D.A. Silva, A.M. Betioli, P.J.P. Gleize, H.R. Roman, L.A. Gómez, J.L.D. Ribeiro, Degradation of recycled PET fibers in Portland cement-based materials, Cement Concr. Res. 35 (2005) 1741–1746, https://doi.org/10.1016/j.cemconres.2004.10.040.
[30] J.-P. Won, C.-I. Jang, S.-W. Lee, S.-J. Lee, H.-Y. Kim, Long-term performance of recycled PET fibre-reinforced cement composites, Constr. Build. Mater. 24 (2010) 660–665, https://doi.org/10.1016/j.conbuildmat.2009.11.003.
[31] R. Rostami, M. Zarrebini, M. Mandegari, D. Mostofinejad, S.M. Abtahi, A review on performance of polyester fibers in alkaline and cementitious composites environments, Constr. Build. Mater. 241 (2020) 117998, https://doi.org/10.1016/j.conbuildmat.2020.117998.
[32] R. Rostami, M. Zarrebini, M. Mandegari, K. Sanginabadi, D. Mostofinejad, S. M. Abtahi, The effect of concrete alkalinity on behavior of reinforcing polyester and polypropylene fibers with similar properties, Cem. Concr. Compos. 97 (2019) 118–124, https://doi.org/10.1016/j.cemconcomp.2018.12.012.
[33] Y. Wang, S. Backer, V.C. Li, An experimental study of synthetic fibre reinforced cementitious composites, J. Mater. Sci. 22 (1987) 4281–4291, https://doi.org/10.1007/BF01132019.
[34] M.E. Fernández, J. Payá, M.V. Borrachero, L. Soriano, A. Mellado, J. Monzó, Degradation process of postconsumer waste bottle fibers used in Portland cement–based composites, J. Mater. Civ. Eng. 29 (2017) 04017183, https://doi.org/10.1061/(ASCE)MT.1943-5533.0002007.
[35] A.H. Ahmed, C. Signorini, M. Chikhradze, M. Liebscher, M. Butler, V. Mechtcherine, Employing limestone and calcined clay for preserving the strain-hardening response of PET fiber-reinforced cementitious composites, Constr. Build. Mater. 438 (2024) 137166, https://doi.org/10.1016/j.conbuildmat.2024.137166.
[36] P. Wang, L. Ke, A.N.S. Sze, Z. Wang, J. Zhao, W. Li, C.K.Y. Leung, Effects of relative humidity, alkaline concentration and temperature on the degradation of plain/coated glass fibers: experimental investigation and empirical degradation model, Constr. Build. Mater. 391 (2023) 131757, https://doi.org/10.1016/j.conbuildmat.2023.131757.
[37] V. Karbhari, W. Chu, Degradation kinetics of pultruded E-glass/vinylester in alkaline media, ACI Mater. J. 102 (2005) 34–41.
[38] H. Jamshaid, H. Ali, R.K. Mishra, S. Nazari, V. Chandan, Durability and accelerated ageing of natural fibers in concrete as a sustainable construction, Material, Materials 16 (2023) 6905, https://doi.org/10.3390/ma16216905.
[39] V. Agopyan, H. Savastano, V.M. John, M.A. Cincotto, Developments on vegetable fibre–cement based materials in São Paulo, Brazil: an overview, Cem. Concr. Compos. 27 (2005) 527–536, https://doi.org/10.1016/j.cemconcomp.2004.09.004.
[40] R.M. de Gutiérrez, L.N. Díaz, S. Delvasto, Effect of pozzolans on the performance of fiber-reinforced mortars, Cem. Concr. Compos. 27 (2005) 593–598, https://doi.org/10.1016/j.cemconcomp.2004.09.010.
[41] G. Mármol, S.F. Santos, H. Savastano, M.V. Borrachero, J. Monzó, J. Payá, Mechanical and physical performance of low alkalinity cementitious composites reinforced with recycled cellulosic fibres pulp from cement kraft bags, Ind. Crops Prod. 49 (2013) 422–427, https://doi.org/10.1016/j.indcrop.2013.04.051.
[42] M. Butler, V. Mechtcherine, S. Hempel, Durability of textile reinforced concrete made with AR glass fibre: effect of the matrix composition, Mater. Struct. 43 (2010) 1351–1368, https://doi.org/10.1617/s11527-010-9586-8.
[43] M. Antoni, J. Rossen, F. Martirena, K. Scrivener, Cement substitution by a combination of metakaolin and limestone, Cement Concr. Res. 42 (2012) 1579–1589, https://doi.org/10.1016/j.cemconres.2012.09.006.
[44] K. Scrivener, F. Martirena, S. Bishnoi, S. Maity, Calcined clay limestone cements (LC3), Cement Concr. Res. 114 (2018) 49–56, https://doi.org/10.1016/j.cemconres.2017.08.017.
[45] J. Sun, F. Zunino, K. Scrivener, Hydration and phase assemblage of limestone calcined clay cements (LC3) with clinker content below 50 %, Cement Concr. Res. 177 (2024) 107417 https://doi.org/10.1016/j.cemconres.2023.107417.
[46] M. Sharma, S. Bishnoi, F. Martirena, K. Scrivener, Limestone calcined clay cement and concrete: a state-of-the-art review, Cement Concr. Res. 149 (2021) 106564, https://doi.org/10.1016/j.cemconres.2021.106564.
[47] B. Kanagaraj, N. Anand, U. Johnson Alengaram, R. Samuvel Raj, S. Karthick, Limestone calcined clay cement (LC3): a sustainable solution for mitigating environmental impact in the construction sector, Resour. Conserv. Recycl. Adv. 21 (2024) 200197, https://doi.org/10.1016/j.rcradv.2023.200197.
[48] P. Haverkamp, M. Traverso, A.H. Ahmed, M. Liebscher, V. Mechtcherine, Evaluating the environmental impacts and social risks of limestone calcined clay cement (LC3) mortars, Sustainability 17 (2025) 8364, https://doi.org/10.3390/su17188364.
[49] E. Berodier, K. Scrivener, Understanding the filler effect on the nucleation and growth of C-S-H, J. Am. Ceram. Soc. 97 (2014) 3764–3773, https://doi.org/10.1111/jace.13177.
[50] W.A. Gutteridge, J.A. Dalziel, Filler cement: the effect of the secondary component on the hydration of Portland cement Part I, A Fine Non-hydraulic Filler 20 (1990) 778–782.
[51] B. Lothenbach, K. Scrivener, R.D. Hooton, Supplementary cementitious materials, Cement Concr. Res. 41 (2011) 1244–1256, https://doi.org/10.1016/j.cemconres.2010.12.001.
[52] A.H. Ahmed, S. Nune, M. Liebscher, T. Köberle, A. Willomitzer, I. Noack, M. Butler, V. Mechtcherine, Exploring the role of dilutive effects on microstructural development and hydration kinetics of limestone calcined clay cement (LC3) made of low-grade raw materials, J. Clean. Prod. (2023) 139438, https://doi.org/10.1016/j.jclepro.2023.139438.

[53] V.G. Papadakis, M.N. Fardis, C.G. Vayenas, Effect of composition, environmental factors and cement-lime mortar coating on concrete carbonation, Mater. Struct. 25 (1992) 293–304, https://doi.org/10.1007/BF02472670.
[54] B. Šavija, M. Luković, Carbonation of cement paste: understanding, challenges, and opportunities, Constr. Build. Mater. 117 (2016) 285–301, https://doi.org/10.1016/j.conbuildmat.2016.04.138.
[55] R. Andersson, H. Stripple, T. Gustafsson, C. Ljungkrantz, Carbonation as a method to improve climate performance for cement based material, Cement Concr. Res. 124 (2019) 105819, https://doi.org/10.1016/j.cemconres.2019.105819.
[56] W. Ashraf, Carbonation of cement-based materials: challenges and opportunities, Constr. Build. Mater. 120 (2016) 558–570, https://doi.org/10.1016/j.conbuildmat.2016.05.080.
[57] M. Zajac, I. Maruyama, A. Iizuka, J. Skibsted, Enforced carbonation of cementitious materials, Cement Concr. Res. 174 (2023) 107285, https://doi.org/10.1016/j.cemconres.2023.107285.
[58] M. Zajac, J. Skocek, J. Skibsted, M.B. Haha, CO2 mineralization of demolished concrete wastes into a supplementary cementitious material – a new CCU approach for the cement industry, RILEM Tech. Lett 6 (2021) 53–60, https://doi.org/10.21809/rilemtechlett.2021.141.
[59] J. Skocek, M. Zajac, M. Ben Haha, Carbon capture and utilization by mineralization of cement pastes derived from recycled concrete, Sci. Rep. 10 (2020) 5614, https://doi.org/10.1038/s41598-020-62503-z.
[60] C.-S. Poon, S. Azhar, M. Anson, Y.-L. Wong, Strength and durability recovery of fire-damaged concrete after post-fire-curing, Cement Concr. Res. 31 (2001) 1307.
[61] R. Snellings, T. Matschei, RILEM TC 309-MCP: recommendation on terminology for mineral carbonation construction products, Mater. Struct. 58 (2025) 1–7, https://doi.org/10.1617/s11527-024-02467-y.
[62] Y. Villagran-Zaccardi, L. Ellwood, P. Perumal, J.M. Torrenti, Z. Zhao, E. Bernard, T. Hanein, T.C. Ling, W. Wang, Z. Zhang, R. Snellings, Carbonated recycled concrete aggregates in construction: potential and bottlenecks identified by RILEM TC 309-MCP, Mater. Struct. 58 (2024) 1–26, https://doi.org/10.1617/s11527-024-02489-6.
[63] W. Hu, D. Zhang, E. Ftwi, B.R. Ellis, V.C. Li, Development of sustainable low carbon engineered cementitious composites with waste polyethylene fiber, sisal fiber and carbonation curing, Resour. Conserv. Recycl. 197 (2023) 107096, https://doi.org/10.1016/j.resconrec.2023.107096.
[64] D. Zhang, B.R. Ellis, B. Jaworska, W.-H. Hu, V.C. Li, Carbonation curing for precast engineered cementitious composites, Constr. Build. Mater. 313 (2021) 125502, https://doi.org/10.1016/j.conbuildmat.2021.125502.
[65] M. Hou, Z. Li, V.C. Li, Green and durable engineered cementitious composites (GD-ECC) with recycled PE fiber, desert sand, and carbonation curing: mixture design, durability performance, and life-cycle analysis, Constr. Build. Mater. 414 (2024) 134984, https://doi.org/10.1016/j.conbuildmat.2024.134984.
[66] Advansa GmbH, PET Advansa, (n.d.). https://www.advansa.com/en/technical-applications/pet/(accessed May 17, 2023).
[67] Y. Li, J. Li, E.-H. Yang, X. Guan, Mechanism study of crack propagation in river sand engineered cementitious composites (ECC), Cem. Concr. Compos. 128 (2022) 104434, https://doi.org/10.1016/j.cemconcomp.2022.104434.
[68] L. Wang, Z. Zhu, A. Hamza Ahmed, M. Liebscher, X. Zhu, V. Mechtcherine, Self-healing behavior of high-strength strain-hardening cement-based composites (HS-SHCC) blended with limestone calcined clay cement (LC3), Constr. Build. Mater. 370 (2023) 130633, https://doi.org/10.1016/j.conbuildmat.2023.130633.
[69] DIN EN 196-1:2016-11, Prüfverfahren für Zement_- Teil_1: Bestimmung der Festigkeit; Deutsche Fassung EN_196-1:2016, 2016, https://doi.org/10.31030/2482416.
[70] I. Curosu, E. Muja, M. Ismailov, A.H. Ahmed, M. Liebscher, V. Mechtcherine, An experimental-analytical scale-linking study on the crack-bridging mechanisms in different types of SHCC in dependence on fiber orientation, Cement Concr. Res. 152 (2022) 106650, https://doi.org/10.1016/j.cemconres.2021.106650.
[71] M. Ranjbarian, V. Mechtcherine, A novel test setup for the characterization of bridging behaviour of single microfibres embedded in a mineral-based matrix, Cem. Concr. Compos. 92 (2018) 92–101, https://doi.org/10.1016/j.cemconcomp.2018.05.017.
[72] A.H. Ahmed, M. Liebscher, V. Mechtcherine, Mechanical performance of strain hardening limestone calcined clay cementitious composites (SHLC4) subject to wet-dry cycles, in: M. Kunieda, T. Kanakubo, T. Kanda, K. Kobayashi (Eds.), Strain Hardening Cem. Compos., Springer International Publishing, Cham, 2023, pp. 3–12, https://doi.org/10.1007/978-3-031-15805-6_1.
[73] A.H. Ahmed, M. Liebscher, V. Mechtcherine, Freeze-Thaw endurance of strain-hardening cementitious composites with low clinker content, in: V. Mechtcherine, C. Signorini, D. Junger (Eds.), Transform. Constr. Adv. Fiber Reinf. Concr., Springer Nature Switzerland, Cham, 2024, pp. 335–343, https://doi.org/10.1007/978-3-031-70145-0_42.
[74] A. Vollpracht, G.J.G. Gluth, B. Rogiers, I.D. Uwanuakwa, Q.T. Phung, Y. Villagran Zaccardi, C. Thiel, H. Vanoutrive, J.M. Etcheverry, E. Gruyaert, S. Kamali-Bernard, A. Kanellopoulos, Z. Zhao, I.M. Martins, S. Rathnarajan, N. De Belie, Report of RILEM TC 281-CCC: insights into factors affecting the carbonation rate of concrete with SCMs revealed from data mining and machine learning approaches, Mater. Struct. 57 (2024) 1–33, https://doi.org/10.1617/s11527-024-02465-0.
[75] S. von Greve-Dierfeld, B. Lothenbach, A. Vollpracht, B. Wu, B. Huet, C. Andrade, C. Medina, C. Thiel, E. Gruyaert, H. Vanoutrive, I.F. Saéz del Bosque, I. Ignjatovic, J. Elsen, J.L. Provis, K. Scrivener, K.-C. Thienel, K. Sideris, M. Zajac, N. Alderete, Ö. Cizer, P. Van den Heede, R.D. Hooton, S. Kamali-Bernard, S.A. Bernal, Z. Zhao, Z. Shi, N. De Belie, Understanding the carbonation of concrete with supplementary cementitious materials: a critical review by RILEM TC 281-CCC, Mater. Struct. 53 (2020) 1–34, https://doi.org/10.1617/s11527-020-01558-w.
[76] Z. Shi, B. Lothenbach, M.R. Geiker, J. Kaufmann, A. Leemann, S. Ferreiro, J. Skibsted, Experimental studies and thermodynamic modeling of the carbonation of Portland cement, metakaolin and limestone mortars, Cement Concr. Res. 88 (2016) 60–72, https://doi.org/10.1016/j.cemconres.2016.06.006.
[77] Z. Liu, W. Meng, Fundamental understanding of carbonation curing and durability of carbonation-cured cement-based composites: a review, J. CO2 Util. 44 (2021) 101428, https://doi.org/10.1016/j.jcou.2020.101428.
[78] X. Pan, C. Shi, X. Hu, Z. Ou, Effects of CO2 surface treatment on strength and permeability of one-day-aged cement mortar, Constr. Build. Mater. 154 (2017) 1087–1095, https://doi.org/10.1016/j.conbuildmat.2017.07.216.
[79] J.J. Chen, J.J. Thomas, H.M. Jennings, Decalcification shrinkage of cement paste, Cement Concr. Res. 36 (2006) 801–809, https://doi.org/10.1016/j.cemconres.2005.11.003.
[80] B. Wu, G. Ye, Development of porosity of cement paste blended with supplementary cementitious materials after carbonation, Constr. Build. Mater. 145 (2017) 52–61, https://doi.org/10.1016/j.conbuildmat.2017.03.176.
[81] S. Zhandarov, C. Scheffler, E. Mäder, U. Gohs, Three specimen geometries and three methods of data evaluation in single-fiber pullout tests, Mech. Compos. Mater. 55 (2019) 69–84, https://doi.org/10.1007/s11029-019-09793-1.
[82] C. DiFrancia, T.C. Ward, R.O. Claus, The single-fibre pull-out test. 1: review and interpretation, Compos. Part Appl. Sci. Manuf. 27 (1996) 597–612, https://doi.org/10.1016/1359-835X(95)00069-E.
[83] S. Zhandarov, E. Pisanova, E. Mäder, Is there any contradiction between the stress and energy failure criteria in micromechanical tests? Part II. Crack propagation: effect of friction on force-displacement curves, Compos. Interfaces 7 (2000) 149–175, https://doi.org/10.1163/156855400300185289.
[84] B. Kottititum, Q.T. Phung, N. Maes, W. Prakaypan, T. Srinophakun, Early age carbonation of fiber-cement composites under real processing conditions: a parametric investigation, Appl. Sci. 8 (2018) 190, https://doi.org/10.3390/app8020190.
[85] G.E. Urrea-Ceferino, D.K. Panesar, H. Savastano, Adjusting curing parameters for innovative and durable vegetable fibre-cement composites, Cem. Concr. Compos. 103 (2019) 121–133, https://doi.org/10.1016/j.cemconcomp.2019.04.028.
[86] L. Gu, D. Kumar, C. Unluer, E.-H. Yang, P.J.M. Monteiro, Investigation of non-uniform carbonation in strain-hardening magnesia composite (SHMC) and its impacts on fiber-matrix interface and fiber-bridging properties, Cem. Concr. Compos. 153 (2024) 105726, https://doi.org/10.1016/j.cemconcomp.2024.105726.
[87] Y. Liu, B. Wu, J. Qiu, A new fiber-bridging constitutive model for quantifying the matrix carbonation and fiber-to-matrix interface healing in PVA fiber-reinforced SHCC, Constr. Build. Mater. 399 (2023) 132548, https://doi.org/10.1016/j.conbuildmat.2023.132548.
[88] G.H.D. Tonoli, V.D. Pizzol, G. Urrea, S.F. Santos, L.M. Mendes, V. Santos, V. M. John, M. Frías, H. Savastano, Rationalizing the impact of aging on fiber–matrix interface and stability of cement-based composites submitted to carbonation at early ages, J. Mater. Sci. 51 (2016) 7929–7943, https://doi.org/10.1007/s10853-016-0060-z.
[89] V.D. Pizzol, L.M. Mendes, H. Savastano, M. Frías, F.J. Davila, M.A. Cincotto, V. M. John, G.H.D. Tonoli, Mineralogical and microstructural changes promoted by accelerated carbonation and ageing cycles of hybrid fiber–cement composites, Constr. Build. Mater. 68 (2014) 750–756, https://doi.org/10.1016/j.conbuildmat.2014.06.055.
[90] G.P. Karayannidis, A.P. Chatziavgoustis, D.S. Achilias, Poly(ethylene terephthalate) recycling and recovery of pure terephthalic acid by alkaline hydrolysis, Adv. Polym. Technol. 21 (2002) 250–259, https://doi.org/10.1002/adv.10029.
[91] S. Ügdüler, K.M.V. Geem, R. Denolf, M. Roosen, N. Mys, K. Ragaert, S.D. Meester, Towards closed-loop recycling of multilayer and coloured PET plastic waste by alkaline hydrolysis, Green Chem. 22 (2020) 5376–5394, https://doi.org/10.1039/D0GC00894J.
[92] E.-H. Yang, V.C. Li, Strain-hardening fiber cement optimization and component tailoring by means of a micromechanical model, Constr. Build. Mater. 24 (2010) 130–139, https://doi.org/10.1016/j.conbuildmat.2007.05.014.
[93] V.C. Li, C.K.Y. Leung, Steady-state and multiple cracking of short random fiber composites, J. Eng. Mech. 118 (1992) 2246–2264, https://doi.org/10.1061/(ASCE)0733-9399(1992)118:11(2246).
[94] C. Lu, V.C. Li, C.K.Y. Leung, Flaw characterization and correlation with cracking strength in engineered cementitious composites (ECC), Cement Concr. Res. 107 (2018) 64–74, https://doi.org/10.1016/j.cemconres.2018.02.024.
[95] G. Gong, M. Guo, Y. Zhou, S. Zheng, B. Hu, Z. Zhu, Z. Huang, Multiscale investigation on the performance of engineered cementitious composites incorporating PE fiber and limstone calcined clay cement (LC3), Polymers 14 (2022) 1291, https://doi.org/10.3390/polym14071291.
[96] Y.-L. Bai, Z.-W. Yan, T. Ozbakkaloglu, Q. Han, J.-G. Dai, D.-J. Zhu, Quasi-static and dynamic tensile properties of large-rupture-strain (LRS) polyethylene terephthalate fiber bundle, Constr. Build. Mater. 232 (2020) 117241, https://doi.org/10.1016/j.conbuildmat.2019.117241.
[97] V. Li, From micromechanics to structural engineering - the design of cementitious composites for civil engineering applications, J. Struct. Mech. Earthq. Eng. 10 (1992) 37–48. http://hdl.handle.net/2027.42/84735.
[98] T. Kanda, Design of Engineered Cementitious Composites for Ductile Seismic Resistant Elements, University of Michigan, Thesis, 1998. http://deepblue.lib.umich.edu/handle/2027.42/131240. (Accessed 2 July 2024).